Compositional Measurements of Saturn's Upper Atmosphere and Rings from Cassini INMS: An Extended Analysis of Measurements from Cassini's Grand Finale Orbits

J. Serigano, S. M. Hörst, C. He, Thomas Gautier, R. V. Yelle, T. T. Koskinen, M. G. Trainer, M. J. Radke

JGR Planets

RESEARCH ARTICLE
10.1029/2022JE007238

Key Points:

- Ion and Neutral Mass Spectrometer returned surprisingly complex mass spectra during final orbits, indicating strong compositional interactions between Saturn and D ring
- We have developed a deconvolution algorithm to handle the complexities of unit resolution mass spectra when calibration data are unavailable
- We attribute a large amount of signal to vaporized ices and organics thought to be flowing into Saturn's atmosphere from the rings

Supporting Information:

Supporting Information may be found in the online version of this article.

Correspondence to:

J. Serigano,
jserigano4@jhu.edu

Citation:

Serigano, J., Hörst, S. M., He, C., Gautier, T., Yelle, R. V., Koskinen, T. T., et al. (2022). Compositional measurements of Saturn's upper atmosphere and rings from Cassini INMS: An extended analysis of measurements from Cassini's Grand Finale orbits. *Journal of Geophysical Research: Planets*, *127*, e2022JE007238. https://doi.org/10.1029/2022JE007238

Received 15 FEB 2022
Accepted 29 APR 2022

Compositional Measurements of Saturn's Upper Atmosphere and Rings From Cassini INMS: An Extended Analysis of Measurements From Cassini's Grand Finale Orbits

J. Serigano[1], S. M. Hörst[1], C. He[1], T. Gautier[2], R. V. Yelle[3], T. T. Koskinen[3], M. G. Trainer[4], and M. J. Radke[1]

[1]Department of Earth and Planetary Sciences, Johns Hopkins University, Baltimore, MD, USA, [2]LATMOS-IPSL, CNRS, Sorbonne Université, UVSQ, Guyancourt, France, [3]Lunar and Planetary Laboratory, University of Arizona, Tucson, AZ, USA, [4]NASA Goddard Space Flight Center, Greenbelt, MD, USA

Abstract The Cassini spacecraft's final orbits sampled Saturn's atmosphere and returned surprisingly complex mass spectra from the Ion and Neutral Mass Spectrometer. Signal returned from the instrument included native Saturn species, as expected, as well as a significant amount of signal attributed to vaporized ices and higher mass organics believed to be flowing into Saturn's atmosphere from the rings. In this paper, we present an in-depth compositional analysis of the mass spectra returned from Cassini's last few orbits. We use a mass spectral deconvolution algorithm designed specifically to handle the complexities involved with unit resolution spaceflight mass spectrometry data to determine the relative abundance of species detected in the observations. We calculate the downward external flux and mass deposition rates of ring volatile species into Saturn's atmosphere and conclude that during these observations ring material was being deposited into Saturn's equatorial region at a rate on the order of 10^4 kg/s.

Plain Language Summary The mass spectrometer aboard the Cassini spacecraft at Saturn directly sampled the region between the planet and its rings. These measurements allow us to infer the chemical composition of the sampled region to better understand what material is present in the region and how Saturn's upper atmosphere and innermost rings interact. The mass spectra returned by the instrument are surprisingly complex and includes signal from vaporized ices and organics, which we attribute to ring material falling into the atmosphere. This material was entering Saturn's atmosphere at a rate on the order of 10^4 kg/s, revealing that the effect of the rings on the atmosphere is more extensive than previously thought. We use this information to infer the composition and amount of material flowing into the Saturn's atmosphere from the rings.

1. Introduction

Among planetary rings in our solar system, Saturn's dynamic ring system shines brightly. The expansive rings provide a unique opportunity to study in close proximity an evolving and structurally complex system akin to many astrophysical disks. Saturn's rings stand out in a compositional sense as well. While other planetary ring systems are composed of primarily dark, dusty material, Saturn's bright, relatively pure, water-dominated rings conjure up questions related to their formation, evolution, and age. However, compositional studies of this diffuse, tenuous region composed of mostly small particles are notoriously difficult. Spectroscopic observations of the rings demonstrate water ice as the main constituent but reveal a spectrum with a steep slope at wavelengths less than 550 nm, indicative of a UV absorbing material intricately mixed with water ice whose origin and composition is still debated (see e.g., Cuzzi, Filacchione, & Marouf, 2018). Recent analysis of spectra taken using HST-STIS of Saturn's rings suggests that a small fraction of the A and B rings could be composed of complex organics along with some silicate and amorphous carbon, likely from meteoritic infall (Cuzzi, French, et al., 2018). Ciarniello et al. (2019) modeled observations from Cassini VIMS and came to a similar conclusion that the ring spectra can be reproduced by water ice grains with the inclusion of organic tholin along with variable amounts of carbon, silicates, or other compounds depending on the ring region observed. Cassini RADAR and observations from VLA, which probe ring particle composition deeper than the surface level, have also provided further evidence of silicates embedded within ring particles (Zhang et al., 2017a, 2017b, 2019).

The Cassini spacecraft's Grand Finale orbits have allowed for in situ analysis of the rings for the first time and revealed that the effect of the rings on the atmosphere is far more extensive than previously thought. These 22

orbits between Saturn and the innermost D ring sampled different altitudes in the region and culminated in atmospheric entry of the spacecraft in September 2017, returning measurements down to a pressure of ∼1 nbar before losing contact with Earth. A number of studies have demonstrated the intricate coupling of the rings and atmosphere from the measurements returned by these final orbits. Ionospheric measurements from the Radio and Plasma Wave Science instrument detected a highly variable electron density as a consequence of the rings casting shadow onto Saturn (Wahlund et al., 2018). Measurements from the Open Source Ion (OSI) mode of the Ion and Neutral Mass Spectrometer (INMS) suggested that the lighter ions detected in Saturn's ionosphere are likely due to the influence of heavier molecules in the region originating from the rings (Cravens et al., 2019), an idea which is also supported through recent ionospheric modeling (Moore et al., 2018). Additional in situ measurements in the region using Cassini's Magnetospheric Imaging Instrument (MIMI) and Cosmic Dust Analyzer (CDA) detected dust grains, water ice, and silicates flowing into the atmosphere from the rings via atmospheric drag due to collisions with H atoms and the dynamical influence of the planet's magnetic field (Hsu et al., 2018; Mitchell et al., 2018). Evidence of ring-atmosphere coupling was first noted during the Voyager era (Connerney & Waite, 1984) and more recently through ground-based observations of H_3^+ variations due to charged water from the rings entering the atmosphere (O'Donoghue et al., 2013, 2017, 2019).

We report here further evidence for strong interactions between Saturn and the D ring using measurements from the Closed Source Neutral (CSN) mode of INMS during the last few orbits of Cassini, which directly measured Saturn's upper thermosphere. These measurements were taken above Saturn's homopause, the level below which an atmosphere is well-mixed and assumes a scale height in accordance with the mean mass of an atmospheric molecule and above which molecular diffusion is a mass-dependent process. As a result, the mass spectra returned from this region were expected to be relatively simple, with contributions from Saturn's native constituents, H_2 and He, and perhaps minor amounts of H_2O from the rings. Instead, recent studies using this data set have reported a surprising amount of nonwater ices and organics also present in the signal. Yelle et al. (2018) reported density profiles of H_2 and He in diffusive equilibrium as expected but also noted a large amount of CH_4 with a nearly constant mixing ratio, indicative of an external inflow from a source beyond the atmosphere. Serigano et al. (2020) expanded on this study to include further evidence of H_2O and NH_3 also infalling into Saturn's atmosphere from the rings. Waite et al. (2018) analyzed the higher mass region of the mass spectra as well, finding that approximately 35% by mass of the inflowing material is organic and that the total mass influx from the rings is on the order of 10^4 kg/s, which was later confirmed by Miller et al. (2020). Comparisons to the inflow rates reported by other instruments suggest that the neutral molecules detected by INMS may be the predominant source of inflowing material from the rings (Perry et al., 2018). However, the surprisingly large inflow rate from the rings is unsustainable over a long period of time when compared to the mass of the ring system, suggesting these observations may be a consequence of a transient perturbation that disrupted the local region and expelled a higher than usual amount of ring material into the atmosphere (Waite et al., 2018).

In this study, we expand on these previous analyses of the mass spectra returned by INMS in the CSN mode and present an independent analysis of the instrument's full mass range using a different approach. We utilize the same mass spectral deconvolution algorithm as our previous paper (Serigano et al., 2020) and detailed in Gautier et al. (2020), which allows us to determine the mixing ratio and density profiles of native and exogenous neutral species found in the spectra. We use these results to calculate the deposition rate of this material into Saturn's atmosphere from the rings. This paper is organized as follows. In Section 2, we present the observations utilized in this study and briefly describe the data reduction process leading to the final mass spectra used for analysis. In Section 3, we describe the mass spectral deconvolution algorithm and explain our database of neutral species used to fit the mass spectra. In Section 4, we present the mass spectral fitting results and compare our best-fitting simulations to the observations. In Section 5, we determine the mixing ratios and densities of the most abundant species in our modeled spectra. In Section 6, we use our results to calculate the downward flux and mass deposition rate (MDR) of external species into Saturn's atmosphere from the rings. Finally, in Section 7, we present a brief summary and conclusions from our analysis.

2. Observations and Data Reduction

2.1. Instrument and Observations

We utilize in situ measurements taken of Saturn's thermosphere using Cassini's INMS operating in the CSN mode during the spacecraft's final orbits around Saturn. Although INMS was originally intended for studies of Titan's upper atmospheric composition (see Serigano et al., 2020 and references therein), the instrument was also used during the Grand Finale orbits to obtain compositional measurements of the region between Saturn and the inner edge of the D ring and multiple studies have already utilized this valuable data set (Miller et al., 2020; Perry et al., 2018; Waite et al., 2018; Yelle et al., 2018). The instrument has a mass range of 1–99 atomic mass units (amu) with a resolving power of 1 amu. A thorough description of the instrument can be found in Waite et al. (2004).

In the CSN mode, INMS is able to directly sample and analyze the neutral composition of the inflowing gas. The sample is ionized by a 70 eV electron beam, resulting in ionized fragments of the neutral parent molecule that are then detected using the instrument. This process produces unique fragmentation patterns for each neutral species based on the composition and structure of the molecule. Thus, the mass spectra returned by INMS is a combination of overlapping signal from all species present in the sample. Determination of the composition of the sample requires accurate knowledge of how each species fragments within the instrument, which can then be used to reconstruct the signal and determine the relative intensities of different species in the measured spectra.

The measurements used here are the same measurements used in Yelle et al. (2018) and Serigano et al. (2020). While these previous studies focused on the lower end of the instrument's mass range (up to 20 amu), this paper encompasses the entirety of the instrument's mass range. We include measurements from Cassini orbits 288, 290, 291, 292, and 293. These orbits comprise the last and deepest orbits of Cassini, which directly sampled Saturn's thermosphere, as well as atmospheric entry, which sampled Saturn down to approximately 1,370 km above the 1-bar pressure level, or approximately 1 nbar. Orbit 289 was not optimized for INMS observations and is not used in this analysis.

The top panels of Figure 1 show some characteristics of the orbits analyzed in this study. All orbits aside from atmospheric entry (orbit 293) probed similar latitudinal and altitudinal regions in close proximity to the ring plane and near the same local solar time. Thus, one would expect the resulting mass spectra from these orbits to be similar, aside from possible differences stemming from dynamical and temporal fluctuations. All orbits sampled the composition of Saturn's isothermal region of the thermosphere aside from atmospheric entry which returned measurements approximately 200 km lower than the other orbits and detected a decrease in temperature with decreasing altitude (Yelle et al., 2018). Additional information about these orbits can be found in Table S1 in Supporting Information S1. The resulting mass spectra from these orbits normalized to m/z 2 for comparison are shown in the lower panel of Figure 1. Mass spectra for all orbits follow a similar trend with slight variations that are likely due to temporal and dynamical fluctuations in the region. For example, the spectrum returned during orbit 291 includes a much larger signal in mass channels attributed to exogenous species while the spectrum returned during atmospheric entry is depleted in these mass channels relative to other orbits. The spectra have strong signal at m/z 2 and 4 as expected because these mass channels represent H_2 and He, the main constituents of Saturn's atmosphere. The spectra also include a surprisingly large signal throughout the entirety of the instrument's mass range. The complex mass spectra include signal from various vaporized ices and organics, which we attribute to ring material falling into the atmosphere and will discuss in detail throughout this analysis.

Due to Saturn's high rotation rate and oblateness, we assume here that atmospheric properties vary with gravitational potential, ϕ, and use this as our vertical coordinate. A detailed description of this approach can be found in Supporting Information of Yelle et al. (2018). The pressure level and the altitude above the 1-bar pressure level that correspond to the gravitational potential field used here can be found on the right y-axis of figures when appropriate. The data used in this analysis can be found in the Planetary Plasma Interactions node of the NASA Planetary Data System public archive (https://pds-ppi.igpp.ucla.edu; Waite et al., 2005).

2.2. Instrument Characterization and Corrections

The data reduction method adopted here is similar to that used in our previous studies of this data set (Serigano et al., 2020; Yelle et al., 2018). Briefly, this includes corrections for saturation of the primary detector, detector

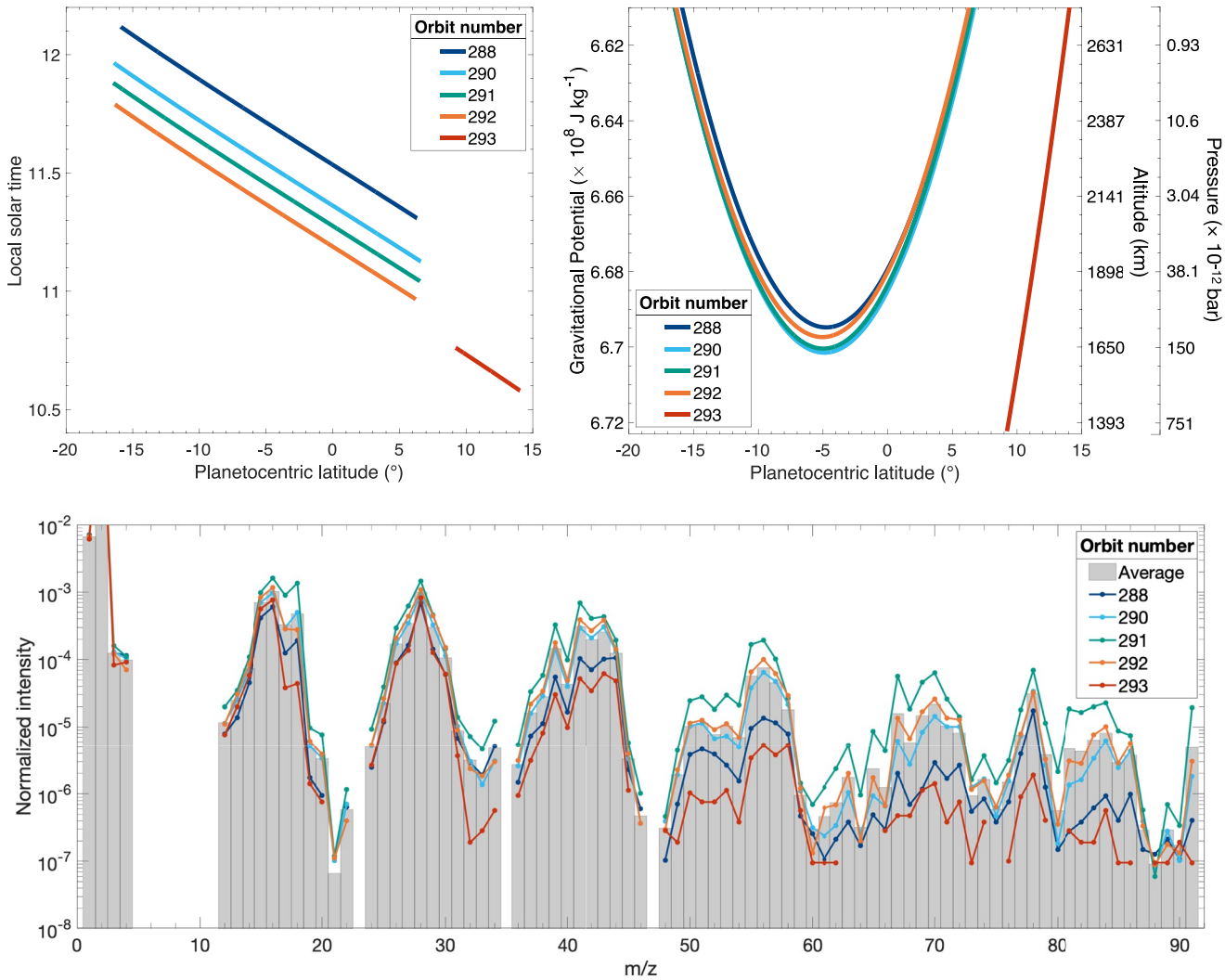

Figure 1. Local solar time (top left) and gravitational potential (top right) as a function of Saturn planetocentric latitude for the Cassini orbits discussed in this analysis. Pressure and altitude above the 1-bar pressure level of Saturn are presented on the right *y*-axis. All orbits aside from orbit 293 (atmospheric entry) occurred during similar conditions. Bottom: Mass spectra for all orbits normalized to H_2 (*m/z* 2) for comparison.

dead-time, ram pressure enhancement, calibration sensitivity, and background subtraction. These corrections are detailed extensively in Section 3.1 of Serigano et al. (2020). We note, as also reported in Waite et al. (2018), Perry et al. (2018), and Miller et al. (2020), that there is no evidence that the speed of the spacecraft during these final orbits (approximately five times faster than typical Titan flybys) had a significant impact on the INMS measurements. Additionally, we do not perform any corrections for thruster firing contamination, which occasionally affected measurements during Titan flybys, as thrusters were not used during the closest approach (C/A) measurements we use here.

Of great concern with INMS neutral measurements is the potential for contamination from previous measurements to create a false signal during subsequent encounters. Particularly, organics from Titan's atmosphere have the potential to adhere to the walls of the INMS antechamber and contribute to the signal of a subsequent encounter at a later time. Contamination from a previous target would culminate in two ways: (a) a similar signal from the contaminating source as compared to the signal detected at the new source, which could correspond to signal from fragmented material that had adhered to the instrument walls, and (b) a larger signal in the contaminated mass channels at the original source as compared to the new source. Figure 2 compares INMS count rates obtained at Saturn during orbit 290 to count rates taken during the Titan T30 flyby, which recorded measurements down to approximately 960 km (~0.5 nbar, similar to pressure conditions at Saturn), and the Enceladus E5 flyby,

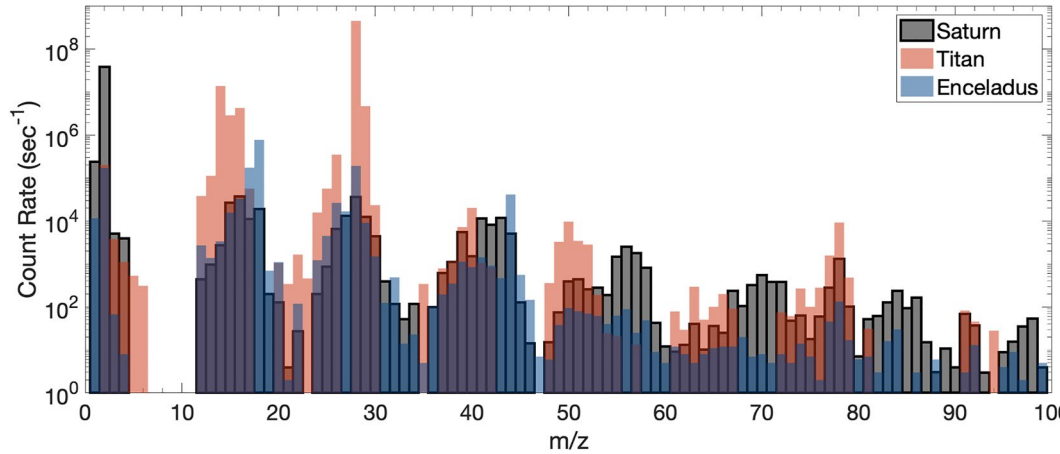

Figure 2. Comparison of Ion and Neutral Mass Spectrometer mass spectra from Saturn (orbit 290, gray), Titan (T30 flyby, red), and Enceladus (E5 flyby, blue). Variation of signal among targets suggests that contamination within the instrument is not significant.

the highest signal to noise encounter of the Enceladus plumes. The mass spectra from different environments are distinct and do not follow similar trends. This is especially notable in the *m/z* ~12–20 region where the highest signal occurs in different mass channels for all encounters: *m/z* 14 at Titan (N_2), *m/z* 16 at Saturn (CH_4 and H_2O), and *m/z* 18 at Enceladus (H_2O). Additionally, at higher masses (>*m/z* ~ 50) where contamination from Titan organics is most likely, the heavier organic signal at Titan deviates significantly from the signal obtained at Saturn. Particularly, the region surrounding the peak near *m/z* 50 at Titan is not present in the Saturn measurements. Additionally, certain regions in the Saturn measurements (near *m/z* 56 and 70) are absent from the Titan observations. Furthermore, inbound INMS measurements taken far from Saturn (>10,000 km above 1 bar pressure level) and far from the equatorial ring plane (near midlatitudes) show no signs of background contamination from residual gas within the instrument, which could be remnants from previous encounters (see e.g., Cui et al., 2009a). Through comparison of these mass spectra at different environments and analysis of INMS measurements far from C/A during these final orbits, we conclude that strong contamination from other sources is unlikely.

As noted in previous studies (see e.g., Cui et al., 2009a; Magee et al., 2009; Teolis et al., 2010), some neutral species are more likely to adsorb on the walls of the antechamber during sampling. This adsorption leads to a time delay in the signal of the adsorbed species and falsely reduces the relative abundance during inbound measurements. Desorption from the chamber walls at a later time leads to an artificial abundance enhancement of that species after the closest approach. Wall sticking predominantly affects outbound measurements, as the adsorbed material begins to desorb after the closest approach and contributes to the signal or chemically reacts with other species within the instrument. Various methods have been used in previous studies to attempt to correct for this issue. Magee et al. (2009) determine a "desorption constant" based on the declining signal of outbound measurements and use an empirical model at Titan in an attempt to remove outbound desorption effects from NH_3. Cui et al. (2009a) assume a species-specific adsorption probability and a desorption time constant in their model to reproduce the observed outbound behavior of heavier species in the instrument. Teolis et al. (2010) develop a more detailed model to correct for water adsorption and desorption during the instrument's encounters with the plumes of Enceladus.

Since INMS outbound measurements are known to suffer more significantly from adsorption issues, our analysis here focuses only on inbound measurements. For this reason, our approach to correct for adsorption and desorption effects within the instrument focuses primarily on inbound adsorption corrections, not outbound desorption corrections. Our analysis does not show any strong evidence of sticking in any mass channels aside from the main parent peaks associated with H_2O (*m/z* 18) and NH_3 (*m/z* 17). Our approach to correct for adsorption includes (a) corrections for the signal time delay of H_2O and NH_3 relative to the signal of all other mass channels and (b) corrections for the artificial reduction in signal due to H_2O and NH_3 sticking to the chamber walls. We use the

following equations for these corrections and assume for simplicity that all of the signal in mass channel 17 is from NH_3 and all of the signal in mass channel 18 is from H_2O.

$$Total(t) = Detected\,(t + t_{des}) + Adsorbed(t) - Desorbed(t) \quad (1)$$

$$Adsorbed(t) = P \times Total(t) \times \left(1 - \frac{\Delta(t)}{S}\right) \quad (2)$$

$$Desorbed(t) = Adsorbed(t - t_{des}) \quad (3)$$

$$\Delta(t) = a \times V \times \sum_{t-t_{des}}^{t} (Total(t) - Detected(t + t_{des}) + Desorbed(t)) \quad (4)$$

where Equation 1 represents the Total, Detected, Adsorbed, and Desorbed number density for each species (cm^{-3}), P is the sticking coefficient for the adsorbing species (~0.5 for H_2O at 300 K; Waite et al., 2009), ~0.4 for NH_3 (Diebold & Madey, 1992), S is the surface area of the chamber walls (11 cm^2; Waite et al., 2004), Δ is the amount of surface area occupied by the adsorbing species, a is the surface area of one molecule of the adsorbing species, and V is the volume of the chamber (3.5 cm^3; Waite et al., 2004). t_{des} is the characteristic time constant for an adsorbing molecule to spend on the chamber walls before desorption, leading to the time delay in signal for adsorbing species. We define this value as the time difference in the maximum count rate between H_2O and NH_3 compared to H_2. As a consequence of sticking, the signal for H_2O and NH_3 peaks on average about 60 s after H_2 and all other species.

Results from our correction for NH_3 (*m/z* 17) and H_2O (*m/z* 18) can be seen in Figure 3 for orbit 290 compared to H_2, He, and *m/z* 15 (a proxy for CH_4), which do not show signs of adsorption. The left figure shows the normalized density for each of these species as a function of time from the closest approach for both inbound (before C/A) and outbound (after C/A) measurements. Prior to correction, H_2O and NH_3 peak approximately 63 s after signal from all other channels. The right figure shows the inbound density profile of the same species. Adsorption corrections to H_2O and NH_3 improve the density enhancement issue at lower altitudes that we noted in our previous paper (Serigano et al., 2020) and also improve the shape of the density profile to more closely follow that of H_2 and CH_4, which is expected for a species with an external source entering the atmosphere. After corrections, the signal in mass channel 17 for the averaged mass spectrum (as seen in Figure 4 for orbit 290 and detailed in the following section) increases by an average factor of 2.32 for orbits analyzed here, and mass channel 18 increases by an average factor of 2.30. These corrections utilize some outbound data to determine t_{des}. Since no outbound data exist for orbit 293 (atmospheric entry), we are not able to perform this correction. Consequently, we use the average correction for all other orbits to correct H_2O and NH_3 during orbit 293 and throughout this paper we include both corrected and uncorrected results for orbit 293. It is possible that the differences in data correction for orbit 293 due to lack of outbound data could be partly responsible for the slope seen in the mixing ratio and density profiles of H_2O and NH_3 in Figures 7 and 8 and discussed later in this analysis. These corrections and the subsequent results reported here represent an important update to our previous work (Serigano et al., 2020), and values presented in this report should be utilized in place of our previous results.

3. Compositional Analysis Techniques

3.1. Mass Spectral Deconvolution

The instrument's unit resolution resolving power complicates the analysis since the fragmented signal of multiple species overlap and contribute to the signals of the same mass channels. Thus, analyzing a complex mixture requires prior knowledge of how each species fragments after ionization within the instrument. These calibration fragmentation patterns can then be used to determine the relative contribution of species to the signal, and ultimately determine the mixing ratios and densities of each species in the sampled region of the atmosphere. Determining the best fitting composition to the data requires solving a system of linear equations:

$$I_i = \sum_{j1}^{n} F_{i,j} N_j \quad (5)$$

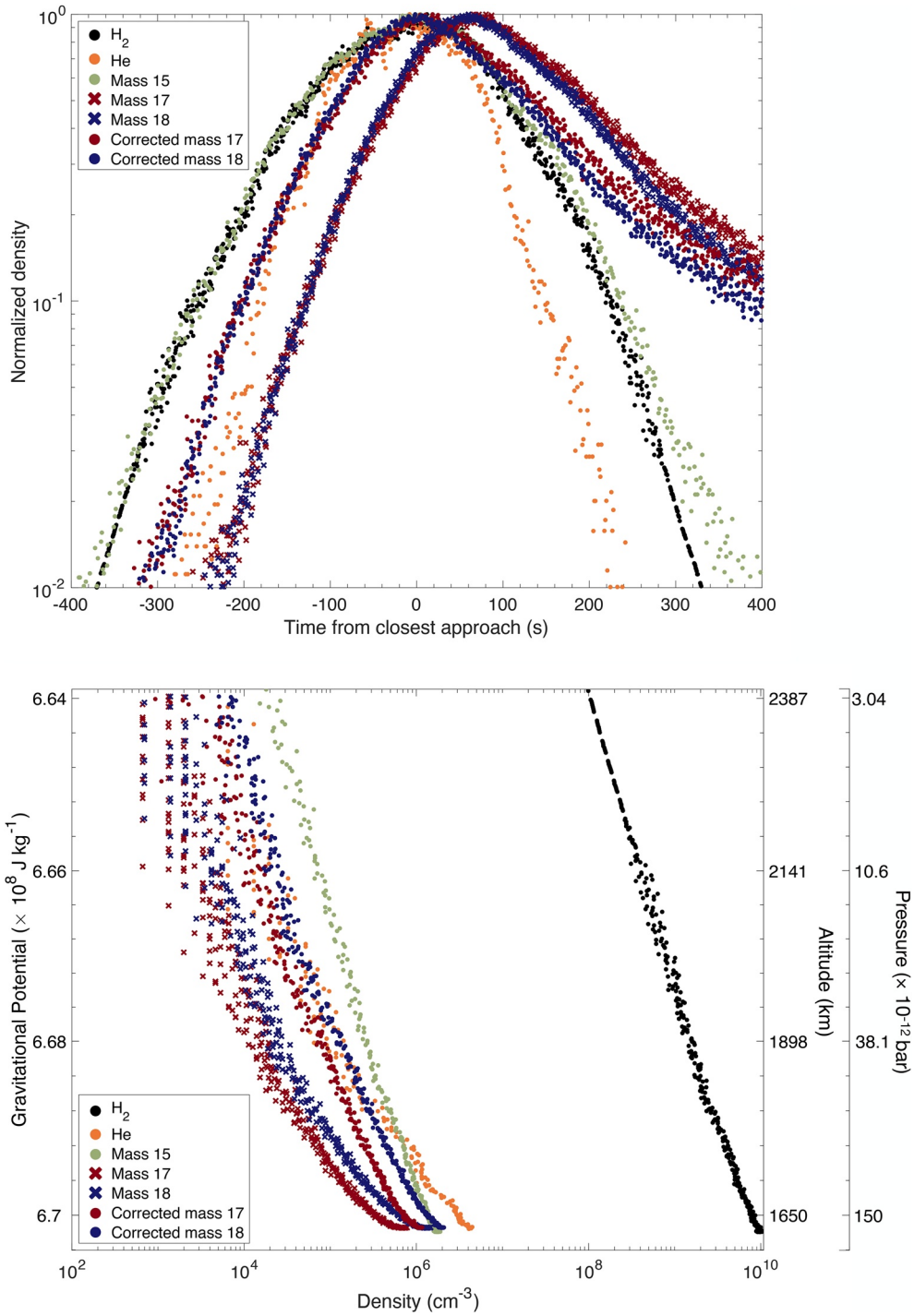

Figure 3. Results of inbound adsorption corrections for NH_3 (*m/z* 17) and H_2O (*m/z* 18) for orbit 290 compared to other species that do not show signs of adsorption issues within the instrument. *m/z* 15 is a proxy for CH_4. Adsorption leads to a time delay in signal for the adsorbing species and an artificial reduction in the relative abundance. Top: Normalized density as a function of time from the closest approach to Saturn's ring plane. Compared to H_2, He, and mass channel 15, the uncorrected signal from mass channels 17 and 18 (red and blue x symbols, respectively) peaks to approximately 60 s after the rest of the signal. After adsorption corrections, mass channels 17 and 18 (red and blue circles) follow a similar trend to channels not affected by adsorption. Bottom: Density results before (x symbols) and after (circles) adsorption corrections for NH_3 and H_2O as compared to other species.

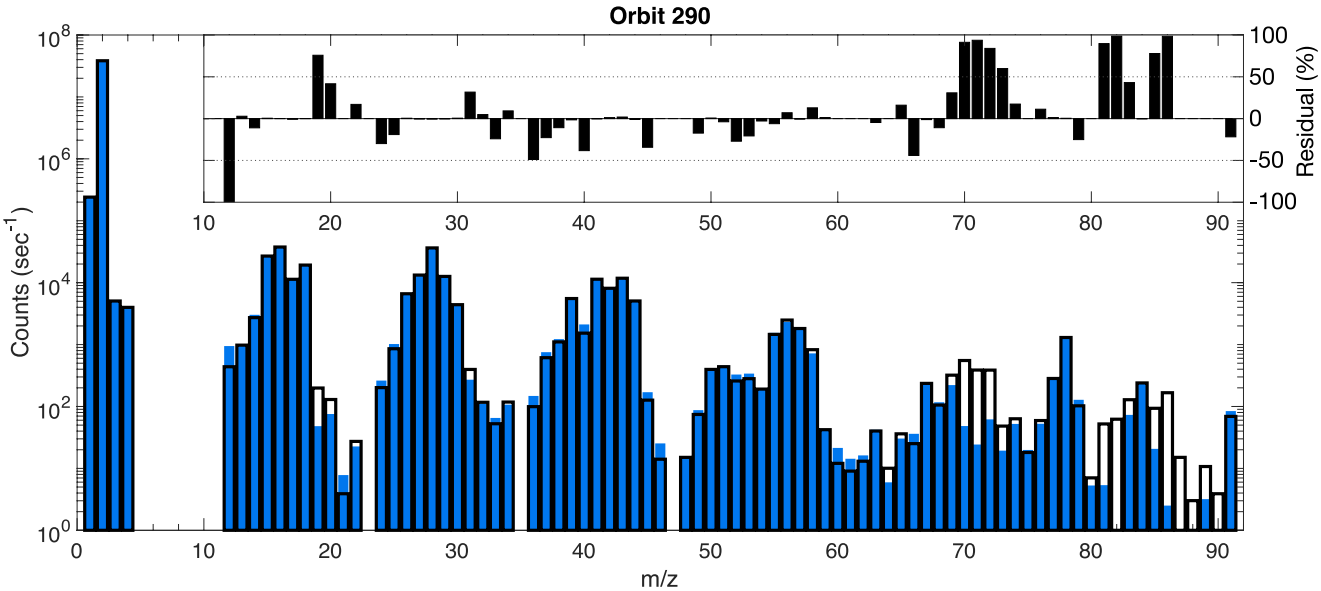

Figure 4. Mass spectral deconvolution result for the averaged mass spectrum returned from orbit 290. Black outline bars represent the measured Ion and Neutral Mass Spectrometer spectrum and blue bars represent the average of the top 10% (50,000) best-fitting simulations. The inset figure in the top right represents the residual to each mass channel. Residuals for mass channels 1–4 are not shown and are always below 1%. Residuals for any mass channel with less than 20 counts are not shown. Fits for other orbits analyzed here can be found in Supporting Information S1.

where I_i is the measured intensity in the mass channel i, $F_{i,j}$ is the fragmentation intensity for species j in the mass channel i, and N_j is the concentration of species j. The relative fragment intensities of a species vary from instrument to instrument, so it is crucial to have a robust calibration database specific to the instrument for mass spectral deconvolution. Unfortunately, this is not always attainable because it is not always known what constituents will be present in an atmosphere before spacecraft arrival and because some gases can be very harmful or difficult to work with in a lab setting. INMS was calibrated for a handful of species relevant to Titan's atmosphere, so we must use fragmentation patterns from a similar instrument as a stand-in when data is unavailable. As an alternative, we use calibration data from the National Institute of Standard and Technology (NIST) mass spectral library (Wallace, 2022) when INMS calibration data does not exist. NIST fragmentation patterns are an acceptable proxy since the ionization energy of the NIST library and INMS are the same (70 eV); however, fragmentation patterns are highly instrument dependent, so the NIST library is not a perfect substitute. Indeed, comparisons to INMS and NIST calibration data, when both are available, show significant deviations mostly in lower intensity fragmentation peaks (Serigano et al., 2020). Furthermore, it is possible that the age of the instrument, which was over 2 decades old at the time of these measurements, could affect the instrument's performance and lead to discrepancies between the existing calibration data and the returned measurements during the Grand Finale orbits.

To deconvolve the mass spectra and overcome the potential issues associated with using a different calibration source or an aging instrument, we use a Monte Carlo-based approach to vary the peak intensity of individual fragment ions for each species. This is the same approach used in Serigano et al. (2020) and detailed in Gautier et al. (2020), with minor modifications (detailed below) to the overall approach to handle the expanded mass range and much larger database of species. Our approach uses an interior-point least-square method that is suitable for large matrices such as the mass spectra we analyze here. The initial calibration database, described below, is a combination of INMS calibration data, when available, and NIST calibration data. We allow fragmentation peak intensities for all species to vary by ±30%, although the best-fitting simulations we save for analysis typically vary less than 15%. When deconvolving the spectra, we save 500,000 simulations and analyze the top 10% (50,000) of these simulations.

INMS returned count rates from Saturn with a large dynamic range, spanning seven orders of magnitude. This complicates residual best fits since mass channels with higher signal dominate the resulting residual. To handle this, we separate the spectra into three different sections and fit each section individually. These sections include (a) the high mass, low signal region (*m/z* 31–36, 46–100), (b) the low mass, high signal region (*m/z* 3–30, 37–45),

and (c) H_2, which has a much higher signal than any other mass channels. The *m/z* 37 to 45 section is included with the lower mass, higher signal region because some of the more prominent species (e.g., CO_2, C_3H_6, C_3H_8) contribute to this region, making the signal here significantly higher than the surrounding mass channels. Since some high mass species have base peaks (the most intense peak of a species after fragmentation) that are much lower in mass than their molecular ion we do not divide the database based solely on location of a species' base peak. If a minor species has a base peak that is overwhelmed by signal from more abundant species, then we use other prominent peaks of considerable intensity to fit these species. For example, the base peak of ethyl cyanide (C_2H_5CN) is *m/z* 28, which is fit mostly by CO and N_2. For this reason, we fit ethyl cyanide using the second most prominent peak, *m/z* 54, which is ∼70% of the intensity of the base peak, and consider the ethyl cyanide part of the high mass region. The fragmentation database is therefore also split up accordingly, with most species added to the appropriate database based on the location of the base peak and some species added to the database that corresponds to a prominent secondary peak as listed in Table 1.

We first deconvolve the high mass region with the relevant database. Although these species have fragmentation peaks at lower masses that contribute to signal outside of this region, we do not include these peaks in the Monte Carlo fitting routine. Instead, after deconvolving the spectra and acquiring the 50,000 best fitting simulations for this region, we use the resulting average fragmentation peak intensity of each species' base peak (or most prominent peak in the region) and the ratio of that peak's intensity to the intensity of peaks outside of the fitting region to determine the contribution of these species to the lower mass channels. Since the lower mass peaks are mostly minor for the species, and since the INMS signal at the higher masses is much lower than the signal at lower masses, these species do not contribute much signal in the lower mass channels. For example, when analyzing the lower mass channels with the highest signal, the higher mass species constitute on average 1.5% of the signal in mass channel 15, 0.1% in channel 16, and 3.6% of the signal in mass channel 28. In total, the high mass species account for 8.4% of the total signal of the lower mass region.

After determining the contribution of the high mass species to the low mass signal, we subtract this contribution and deconvolve the remaining low mass signal using the appropriate portion of the database, again saving the 50,000 best-fitting simulations for analysis. Results for the high mass fit, low mass fit, and H_2 are combined before analysis. Similar to Serigano et al. (2020), we perform this analysis on the data in two different forms: (a) an averaged mass spectrum for each orbit that allows us to directly compare the results from all orbits, and (b) binned mass spectra for each orbit that allow us to retrieve mixing ratio and density profiles. The averaged mass spectra consist of data from the region of Saturn's atmosphere where reliable data exists for all orbits, which include measurements taken between ϕ of 6.69 and 6.66×10^8 J kg^{-1} (∼1,700–2,050 km). The binned mass spectra are divided into regions with a width of $\phi = 0.01 \times 10^8$ J kg^{-1} and the deconvolution is performed separately on each bin.

3.2. Database

The fragmentation pattern database used in this analysis includes 80 species, which can be found in Table 1. Since the detected material is thought to derive from Saturn's rings, our decision to include species in the database is determined by the current understanding of the volatile composition of diffuse environments in the outer solar system as well as the signal returned from INMS itself. Diffuse environments include comets (see e.g., Goesmann et al., 2015), Pluto (Grundy et al., 2016), and icy moons including Enceladus (Waite et al., 2009), Triton (Cruikshank et al., 1993), and the upper atmosphere of Titan (see e.g., Cui et al., 2009a; Hörst, 2017). These environments provide evidence of organic compounds in comets and at Enceladus as well as many complex hydrocarbons (HC) and nitriles seen in Titan's N_2/CH_4-rich atmosphere. The most prominent species in our database include the native components of Saturn, H_2, HD, and He, and the most abundant ices of the outer solar system, H_2O, NH_3, CH_4, CO, N_2, and CO_2, all of which have fragmentation patterns that are compatible with the returned INMS signal. UV irradiation and other dissociative processes of these ices, including the ablation of icy grains as they enter the atmosphere (Hamil et al., 2018), provide plausible formation pathways to a variety of HC and nitrogen- or oxygen-bearing species that we also include in the database. Some heavier molecular formula in the database include many stable isomers. Including all stable isomers would lead to a significant and unattainable increase in computational time and complicate model output. Consequently, we only include isomers that are stable and are mostly likely to exist in this region. Fragmentation pattern intensities differ among isomers; however, molecular formula with multiple stable isomers occur only at higher masses and these species have low

Table 1
Species Included in Our Database

Species name	Species formula	Base peak (amu)	Ionization cross-section (Å^2)	Calibration source
Hydrogen	H_2	2	1.54	INMS
Low mass, high signal species				
Hydrogen deuteride	HD	3	1.74	INMS
Helium	He	4	0.33	NIST
Ammonia	NH_3	17	3.47	NIST
Methane	CH_4	16	4.43	INMS
Water	H_2O	18	2.64	INMS
Acetylene	C_2H_2	26	4.40	INMS
Hydrogen cyanide	HCN	27	3.44	INMS
Nitrogen	N_2	28	2.48	INMS
Carbon monoxide	CO	28	2.61	NIST
Ethylene	C_2H_4	28	5.86	INMS
Ethane	C_2H_6	28	7.32	INMS
Formaldehyde	H_2CO	29	4.07	NIST
Acetaldehyde	C_2H_4O	29	6.96	NIST
Propane	C_3H_8	29	10.2	INMS
Methylamine	CH_5N	30	6.36	NIST
Ethylamine	C_2H_7N	30	9.25	NIST
Argon	Ar	40	2.77	INMS
Allene	CH_2CCH_2	40	7.29	INMS
Propyne	CH_3CCH	40	6.56	INMS
Ethylenimine	C_2H_5N	40	7.79	NIST
Acetonitrile	CH_3CN	41	6.33	INMS
Propene	C_3H_6	41	8.75	NIST
Ketene	C_2H_2O	42	5.50	NIST
Acetone	C_3H_6O	43	9.85	NIST
Butane	C_4H_{10}	43	13.1	NIST
Isobutane	C_4H_{10}	43	13.1	NIST
Pentane	C_5H_{12}	43	16.0	NIST
Isohexane	C_6H_{14}	43	18.9	NIST
Carbon dioxide	CO_2	44	3.71	INMS
Dimethylamine	C_2H_7N	44	9.25	NIST
Dimethyl ether	C_2H_6O	45	8.42	NIST
Formamide	CH_3NO	45	6.00	NIST
Isopropyl alcohol	C_3H_8O	45	11.3	NIST
High mass, low signal species				
Ethyl cyanide	C_2H_5CN	28 (54)	9.22	INMS
Formic Acid	CH_2O_2	29 (46)	5.17	NIST
Ethyl isocyanide	C_3H_5N	29 (55)	9.22	NIST
Glyoxal	$C_2H_2O_2$	29 (58)	6.60	NIST
Ethanol	C_2H_6O	31	8.42	NIST
Hydroxy-acetaldehyde	$C_2H_4O_2$	31	8.06	NIST
Methyl formate	$C_2H_4O_2$	31	8.06	NIST

Table 1
Continued

Species name	Species formula	Base peak (amu)	Ionization cross-section (Å^2)	Calibration source
1-propanol	C_3H_8O	31	11.3	NIST
1,2-ethanediol	$C_2H_6O_2$	31	9.52	NIST
Methyl alcohol	CH_4O	31	5.53	NIST
Oxygen	O_2	32	2.28	NIST
Hydrogen sulfide	H_2S	34	5.34	NIST
Phosphine	PH_3	34	4.18	NIST
1,3-butadiene	C_4H_6	39 (54)	10.2	INMS
1-butene	C_4H_8	41 (56)	11.6	NIST
Acetic acid	$C_2H_4O_2$	43 (60)	8.06	NIST
2-methyl-butane	C_5H_{12}	43 (57)	16.0	NIST
Hydroxylamine, O-methyl-	CH_5NO	47	7.46	NIST
Diacetylene	C_4H_2	50	7.26	INMS
Propiolonitrile	C_2HCN	51	6.30	INMS
Cyanogen	C_2N_2	52	5.34	INMS
1-buten-3-yne	C_4H_4	52	8.72	NIST
Acrylonitrile	C_2H_3CN	53	7.76	INMS
2-propynal	C_3H_2O	53	6.93	NIST
2-propenenitrile	C_3H_3N	53	7.76	NIST
3-methyl-1-butene	C_5H_{10}	55	14.5	NIST
2,3-dimethyl-2-pentene	C_7H_{14}	55	20.3	NIST
Propargyl alcohol	C_3H_4O	55	8.39	NIST
1-hexene	C_6H_{12}	56	17.4	NIST
2-propenal	C_3H_4O	56	8.39	NIST
2,2-dimethyl propane	C_5H_12	57	16.0	NIST
Propanal	C_3H_6O	58	9.85	NIST
Methylamine, N,N-dimethyl-	C_3H_9N	58	12.1	NIST
Acetaldoxime	C_2H_5NO	59	8.89	NIST
Formamide, N-methyl-	C_2H_5NO	59	8.89	NIST
Acetamide	C_2H_5NO	59	8.89	NIST
Methanamine, N-methoxy-	C_2H_7NO	61	10.4	NIST
1,3-cyclopentadiene	C_5H_6	66	11.6	NIST
Trans-1,3-pentadiene	C_5H_8	67	13.1	NIST
Pyrrole	C_4H_5N	67	10.7	NIST
Furan	C_4H_4O	68	9.82	NIST
Benzene	C_6H_6	78	13.0	NIST
Pyridine	C_5H_5N	79	12.1	NIST
E,E-1,3,5-heptatriene	C_7H_{10}	79	17.4	NIST
o-xylene	C_8H_{10}	91	18.8	NIST
Toluene	C_7H_8	91	15.9	INMS

Note. Mass spectra are fit in three separate sections: (a) H_2, (b) the low mass, high signal region (*m/z* 3–30, 37–45), and (c) the high mass, low signal region (*m/z* 31–36, 46–100). Species in this table are separated according to the region. Species with multiple base peaks listed are fit using a predominant peak (in parenthesis) that is not the base peak to include these species in the high mass, low signal region (see text for further description).

abundances and small contributions to the overall fit of the mass spectra. H_2 and HD are the only isotopologues that we separate and treat as individual species in our analysis since INMS was calibrated for these separately. Since these measurements are taken above the homopause, HD will have less of a vertical extent in the atmosphere as compared to H_2 and separating these species allows us to retrieve a more accurate density profile of HD in this region. ^{3}He, which has the same mass as HD and would also contribute to the signal in mass channel 3, is not included in this study. The ^{3}He/^{4}He isotopic ratio is on the order of 10^{-6}, so ^{3}He would provide at most a few counts to the signal in mass channel 3. Additionally, the peak intensity for ^{3}He does not exist in the available NIST and INMS calibration data.

Although the INMS mass range extends to *m/z* 99, our database and modeling efforts focus mainly on lower masses with much higher signal. We include only five species in our database with base peaks above 70 amu since most of the signal above 70 amu is significantly weaker than the rest of the spectrum. Adding additional heavier species complicates the deconvolution and significantly increases computational time without significant improvement to the overall fit. Furthermore, it is possible that some of the signal in the instrument's mass range comes from fragmented pieces of molecules with masses exceeding the instrument's mass range. We do not include species with signal above the mass range of the instrument; however, as it is likely that any contribution of larger species is not very significant. In fact, other Cassini instruments with mass ranges higher than INMS reported a much smaller influx of material in this region, suggesting that the ring material entering Saturn's atmosphere may be predominantly smaller molecules such as those measured by INMS. The MIMI, which measures particles in the mass range 8,000–40,000 amu, reported a MDR of about 5.5 kg/s (Mitchell et al., 2018) while the CDA, which measures even larger nanograins, reported a MDR on the order of 10^2–10^3 kg/s (Hsu et al., 2018). Both of these instruments measured ring material inflow at much lower rates than INMS ($>10^4$ kg/s, discussed below). We include toluene (C_7H_8) and o-xylene (C_8H_{10}) as our highest mass species, both with base peaks at *m/z* 91 and use this base peak as the end of our mass range. Due to a lack of species in our database with higher mass fragments, mass channels above ∼70 amu display a larger amount of underfit peaks. As a consequence, our modeling efforts may return larger abundances for these higher mass species since we do not include many other species that might contribute to the signal in this region.

4. Mass Spectral Deconvolution Result

An example of the resulting best fit for averaged data from orbit 290 is shown in Figure 4. The fits for all orbits follow a similar trend and can be found in Figure S1 in Supporting Information S1. The blue mass spectrum represents the average of the top 10% best-fitting simulations, the black outline bars represent the measured INMS spectrum, and the inset figure represents the residual to each mass channel fit. Residuals for mass channels 1–4, which are not shown in this figure, are always below 1%. Residuals for any mass channel with less than 20 counts are not shown as these mass channels do not contribute significantly to the overall fit of the spectrum.

Our simulated mass spectra for all mass channels with counts above 10^3, which make up on average 94.5% of the non-H_2 signal, are fit to be within 1.95% and mass channels with counts above 10^4 (70.1% of the non-H_2 signal) are fit to be within 0.38% percent. These values exclude H_2, which dominates the signal, and is always fit to be within 0.001%. Although isotopic values can be deduced from our best fitting models, we do not report any isotopic measurements in this analysis since these measurements were taken in Saturn's diffuse uppermost atmosphere, which makes it difficult to discern any meaningful isotopic information. Probability density functions, which allow us to quantify the variation in a species' concentration throughout the best-fitting simulations, are also included in Figures S2–S6 in Supporting Information S1 for all averaged orbits.

We allow fragment intensities to vary by ±30%; however, the final results for the most significant fragments vary only by a few percent from the original reference fragment intensity from NIST or INMS calibration data. Figure 5 shows an example of the typical variation of fragmentation peak intensities for CH_4, H_2O, and NH_3 for orbit 290, which are three of the most abundant species detected in the spectra and have overlapping fragmentation patterns. Intensities (in arbitrary units) are normalized to the base peak. The original (red) data point refers to the original fragmentation intensity of each peak in the starting database and the median (white) data point refers to the median intensity of the best-fitting 50,000 simulations. The width of the shaded gray region represents the probability density of all 50,000 best-fitting simulations and the black bars represent one standard deviation of the results. In most instances the higher intensity fragments, which contribute more to the overall

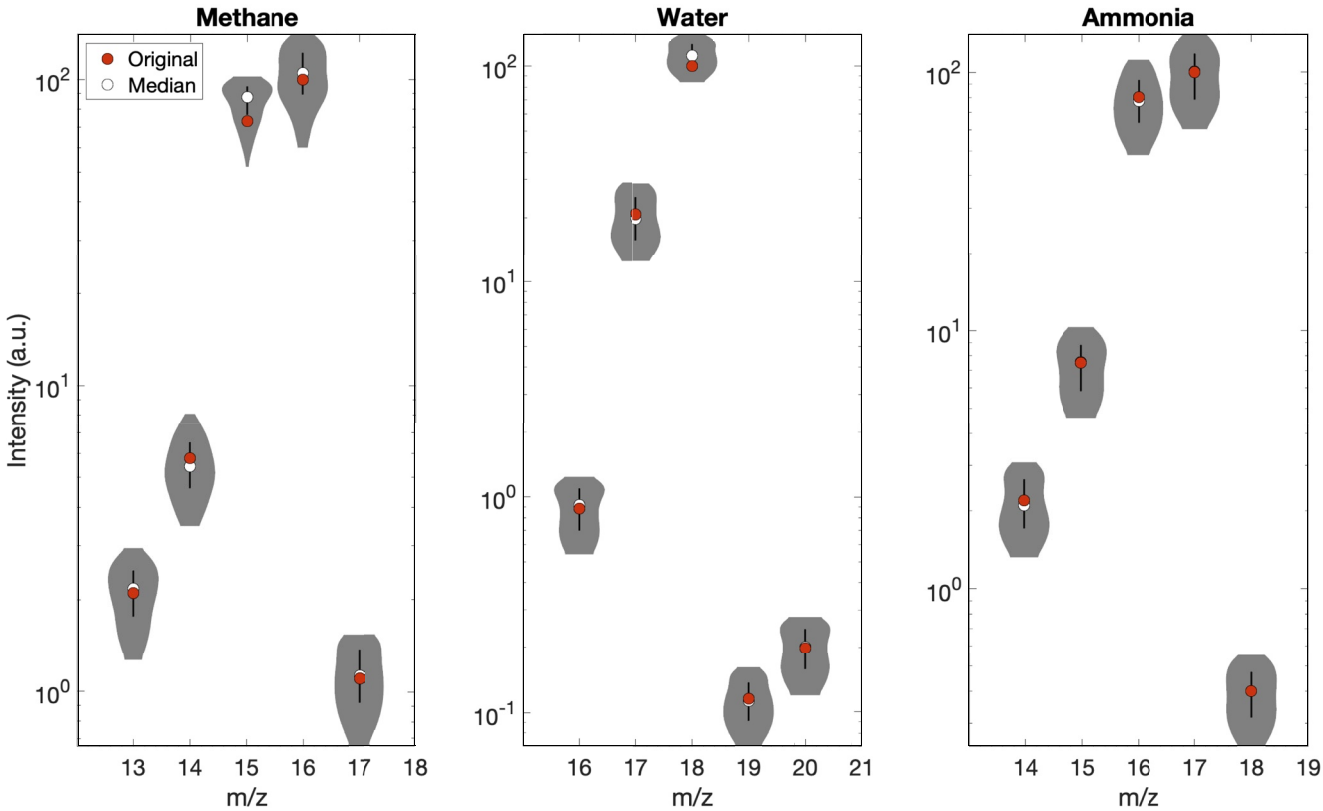

Figure 5. Example of fragmentation peak intensity variations for CH_4, H_2O, and NH_3 for orbit 290. The original (red) data point refers to the original fragmentation intensity of each peak in the starting database and the median (white) data point refers to the median intensity of the best-fitting 50,000 simulations. The width of the shaded gray region represents the probability density of all 50,000 best-fitting simulations and the black bars represent one standard deviation of the results.

signal and residual, vary more than their lower intensity counterparts. For example, the two highest intensity peaks for CH_4, *m/z* 15 and 16, vary on average 15% and 11%, respectively, for all orbits, whereas *m/z* 13 and 14 vary by 1.7% and 1.4%, respectively.

Variations in the peak intensities due to our Monte Carlo fitting routine are moderate but do have a noticeable impact on the resulting abundances. To assess our modeling efforts, we perform an additional simulation for each mass spectra using the original database (i.e., the starting database with no randomization of the fragmentation pattern intensities). The lack of variations leads to a poorer fit overall, with non-H_2 counts above 10^3 fit to be within 8.57% and counts above 10^4 fit to be within 1.83%. The mixing ratios of species, which will be discussed in the follow section, are also affected. For example, the mixing ratio of CH_4 increases on average by 25.6% when using the original database, while H_2O increases by 25.4%, and NH_3 increases by 16.1%. Mixing ratio results for all species from our modeling efforts can be found in Table S2 in Supporting Information S1. A comparison of the results using the original database with no Monte Carlo variations compared to our modeled results for orbit 290 can be found in Table S3 in Supporting Information S1.

Fitting a unit resolution mass spectrum whose signal is a combination of many different species is a degenerate process with many plausible solutions. The 80 species used in our model could plausibly exist in the environment where these measurements were recorded and all contribute to the resulting spectral fit; however, it is not possible to definitively identify most species due to the overlapping nature of fragmentation patterns in unit resolution mass spectra. Thus, we report here our best understanding and interpretation of the signal returned by the instrument based on our best fitting models and present a set of species for which the combination of relative intensities and fragmentation patterns are consistent with the measured mass spectra. To evaluate the importance of individual species to the overall fit, we omit one species from the database and model the spectrum again without that species contributing to the fit. We use the Akaike information criterion (AIC), which balances the goodness of fit

Table 2
Akaike Information Criterion Values

Species omitted	AIC value
Hydrogen	1.47×10^{15}
Hydrogen deuteride	2.55×10^{7}
Helium	1.59×10^{7}
Water	2.21×10^{5}
Methane	1.34×10^{5}
Ammonia	2.39×10^{4}
1-hexene	7.58×10^{3}
Propene	7.08×10^{3}
2-propenal	7.00×10^{3}
Carbon dioxide	6.98×10^{3}
2,2-dimethyl propane	6.94×10^{3}
Propane	6.90×10^{3}
Propanal	6.74×10^{3}
Baseline	6.68×10^{3}
Remaining species	$6.43–6.65 \times 10^{3}$

$\left(\chi^2_{\min}\right)$ with the total number of independent parameters in the model, to evaluate how well the modeled spectra fit the data after removing one species and compare these values to the baseline AIC value, which includes all 80 species in the database. Thus, an AIC value lower than the baseline AIC value indicates a better fitting model. An AIC value that is higher than the baseline AIC value indicates that the species that was removed from the database provides an important contribution to the fit. The AIC equation is given by

$$AIC = \chi^2_{\min} + 2K \quad (6)$$

where K is the number of independent parameters within the model, which includes the number of species in the database as well as the number of fragmented peaks for all species. AIC values for orbit 290 are shown in Table 2. Only models with AIC values above the baseline value are reported. The AIC values for all remaining species are similar to that of the baseline model and the range of AIC values for these species is reported here for simplicity. H_2, HD, and He provide the most important contributions to the modeled spectra and omitting these species results in a severely worse fit to the data. CH_4, H_2O, and NH_3 also provide important contributions to the spectral fit between 12 and 20 amu, which cannot be compensated for when these species are omitted. The other species with AIC values above the baseline contribute significantly to regions of the mass spectrum near 29, 40, and 56 amu. Given the methodology of our spectral fitting procedure, omitting certain species from the database still leads to an acceptable fit since fragments of other species are able to compensate for the loss of contribution from the omitted species. Thus, an AIC value at or slightly below the baseline AIC value does not indicate a nondetection. For example, although CO and N_2 contribute significantly to our best fitting models and are likely present in the spectra, omitting one or the other of these species still leads to a good fit that is comparable with our baseline model. Since we do not include many species with base peaks above 70 amu, the species that do have base peaks above 70 amu produce deceptively large AIC values when omitted. For this reason, we only consider the fit below 70 amu when calculating AIC values and do not report AIC values for the species with base peaks above 70 amu: benzene, pyridine, E,E-1,3,5-heptatriene, o-xylene, and toluene.

Given the location of these measurements, it is possible that part of the signal measured by INMS is due to solid phase ring particles such as dust or ice grains entering the instrument and fragmenting on impact. This would result in signal from fragmented or vaporized dust particles that would be interpreted as gas inflowing into Saturn. Miller et al. (2020) infer a gas to dust molar ratio between 0.74 and 2.24 using arguments related to species volatility and the distribution of signal during higher altitude passes. Due to the observational difficulties of determining the dust composition and number density of D ring dust in this region it is not straightforward to quantify the dust to gas molar ratio with such limited observations. The only in situ dust observations that exist measured nanograin compositions of water ice and silicates, different in composition from the organics that comprise a large part of the INMS signal (Hsu et al., 2018). INMS measurements also show no evidence of grain impacts in the instrument during the orbits analyzed here. Grain impacts during Enceladus plume encounters created notable spikes in the signal due to grains being vaporized on impact with the instrument's antechamber walls (Teolis et al., 2010). Although we believe the signal analyzed here is mostly a product of gas in the region, determining the gas to dust molar ratio is highly speculative due to limited observations in this region and we do not attempt to quantify this ratio here.

4.1. Mass 1–20

The mass range from *m/z* 1–20 was the focus of Serigano et al. (2020). Our previous analysis used only H_2, He, CH_4, H_2O, and NH_3 to fit this region of the spectrum. Our present analysis uses 80 species, many of which contribute to the signal in this region and modify the contribution of CH_4, H_2O, and NH_3 to these channels.

Additionally, H_2 and HD, which we considered as one combined species in our previous study, are separated in this analysis to retrieve a density profile for HD.

Results for H_2 and He agree with our previous analysis. CH_4 results are also similar to those in our previous study, although contributions from CH_4 have decreased slightly in our new analysis due to fragments of higher mass species contributing to mass channels associated with CH_4. In Serigano et al. (2020), CH_4 accounted for 98% of the signal in mass channel 15% and 91% of the signal in mass channel 16. In our current analysis, CH_4 accounts for 90% and 83% of the signal in these channels. Due to the adsorption corrections described earlier, results for H_2O and NH_3 are not directly comparable between our studies. The signal in mass channels 17 and 18, the main peaks associated with NH_3 and H_2O, increased twofold after corrections and the contributions of NH_3 and H_2O to these channels did as well. The variability in abundance for these species noted in our previous analysis is still present and will be discussed in the following section.

While the most prominent peaks always fit very well in this region, mass channel 12, which is always on the order of 10^2 counts, is a minor peak in our analysis that is consistently overfit by our model. When comparing species that are present in both data sets, the peak intensity in mass channel 12 is typically much higher in the NIST calibration data than it is for the INMS data. For example, the peak intensities for mass channel 12 for CH_4 and CO_2 are 6.3 and 7.3 times higher, respectively, in the NIST calibration data. Since NIST data must be used for many carbon-bearing species, the tendency of NIST calibration data to be higher than that of INMS in mass channel 12 could be partially responsible for the discrepancy between the measured spectra and our best-fitting simulations. Our best-fitting scenario for orbit 290 over-predicts the signal in mass channel 12 by a factor of 2.1, with 35% of that signal attributed to carbon-bearing species for which NIST calibration data is used. If we reduce these peak intensities by a factor of 6, as is the approximate difference between INMS and NIST data for CH_4, the resulting fit drops to an overprediction of a factor of 1.5. This overprediction is more in line with the fitting of other peaks with intensity on the order of 10^2.

The signal in mass channels 19 and 20 are consistently underfit and always slightly elevated near C/A. For mass channel 19, this includes C/A during orbits that sampled the less dense outer F ring and regions higher in altitude than the deepest orbits discussed here (found in Figure S7 in Supporting Information S1). The signal in mass channels 19 and 20 could be attributed to certain species, including Ar and H_2O, but even with contributions from these species the signal still remains underfit. Isotopes of H_2O are responsible for the H_2O contributions to these channels (in the form $H_2^{17}O$ in *m/z* 19 and $H_2^{18}O$ in *m/z* 20); however, the level of isotope enrichment needed to fit these peaks is unlikely. The Ar abundance that would be needed to fit these peaks is also unlikely in this region. It is possible that mass channel 19 suffers from internal instrument contamination from filament desorption (see e.g., Perry et al., 2010, 2015). Fluorosilicone o-rings are commonly used in spacecraft and fluorine outgassing could contribute to the signal in mass channel 19; however, this is a poorly constrained source of contamination. The high signal associated with mass channel 20 might also be associated with fluorine contamination. Fluorine is the most electronegative element, meaning it is possible that any fluorine in the antechamber readily reacts with hydrogen to form HF, which would contribute to mass channel 20.

4.2. Mass 28

The signal at mass channel 28 is significant and the potential species contributing to this channel could have major implications for the inner ring composition. N_2 and CO both share *m/z* 28 as their base peak and stand out as prominent volatile ices with abundant reservoirs on airless bodies throughout the outer solar system. This makes their presence in the rings plausible; however, no ring composition studies to date have definitively detected these volatiles in the rings. C_2H_4 and C_2H_6 are additional organics with plausible formation pathways in this region that could also have significant contributions to mass channel 28. The degeneracy involved with deconvolving the signal in mass channel 28 is further complicated by the lack of notable fragmentation peaks for these species in other mass channels. For example, the next most prominent peaks for CO include mass channels 12 and 16, both of which are overwhelmed by signal from other species. Similarly, the next most prominent peak for N_2, mass channel 14, is swamped by signal from fragments of CH_4 and NH_3. Without higher resolution data, which would allow for unique identification, we must rely on our modeling efforts and careful analysis of the deconvolution to determine the best fitting results to these measurements. Our best fits for all orbits have a similar contribution from both N_2 and CO to mass channel 28, with less of a contribution from C_2H_4, C_2H_6, and other

organics contributing to the mass channel. On average, CO contributes 37% to the total signal at mass 28, while N_2 contributes 34% percent, C_2H_6 contributes 10%, and C_2H_4 contributes 7%, with the remaining 12% attributed to other species.

4.3. Other Masses

As previously noted, the complexity of the mass spectra returned by INMS was unexpected and the higher mass organic signal was particularly surprising. HC, nitriles, oxygen-bearing species, and higher mass organics all have significant contributions in our modeled spectra, with a handful of species in the database comprising the majority of the remaining signal. The bulk of the signal surrounding mass channel 28 is dominated by HCN, C_2H_2, and H_2CO. The following region, around $m/z \sim 40$, is dominated by C_3H_6, C_3H_8, C_2H_4O, and CO_2, with additional contributions from fragments of butane and isobutane (isomers of C_4H_{10}). Above this region, the signal is dominated mostly by four species: benzene (C_6H_6), 1-hexene (C_6H_{12}), 2-propenal (C_3H_4O), and 2-methyl-butane (C_5H_{12}), which make up 60.1% of the higher mass contribution on average.

The unexpected complexity of the mass spectra leads one to question the origin of this material. Although they have never been detected in the rings before, the existence of native ices other than H_2O (e.g., CH_4, NH_3, CO, N_2, and CO_2) is likely. In fact, INMS measured other regions of the rings and found additional evidence of non-water ices. These measurements include spectra from the F ring-grazing orbits (C/A ~2.47 R_S) as well as middle (C/A ~2,840 km) and high (C/A ~3,400 km) altitude orbits between Saturn and the D ring. Spectra from these orbits are much lower in signal; however, mass channels that are consistently above the noise level include channels associated with H_2, CH_4, 28 amu (mostly CO/N_2), and CO_2. This signal, along with the density profile of these species at lower altitudes matching that of H_2, suggests that this ring material is likely the external source for the material falling into Saturn's atmosphere. These spectra can be found in Figure S7 in Supporting Information S1. The difficulty of remotely measuring the diffuse, tenuous rings may have allowed these volatiles to elude detection until now. Additionally, Saturn's D ring is dustier than the other main rings, indicating that the D ring has a higher concentration of non-water ice material (Cuzzi, Filacchione, & Marouf, 2018). The higher mass constituents, on the other hand, could be native to the rings or could potentially be products of photochemistry.

Photodissociation of CH_4 in Titan's thermosphere is responsible for the organically rich atmosphere found there (see e.g., Hörst, 2017). Similar to Titan, EUV photons, high energy electrons from Saturn's magnetosphere, and other energetic particles needed for photochemistry are also present in Saturn's upper atmosphere and rings. Downward diffusion time scales are significantly shorter than photochemical timescales in Saturn's upper thermosphere, where these measurements were taken, so any significant photochemistry is unlikely in this region. This exogenous material, however, could play an important role in photochemistry and composition deeper in Saturn's atmosphere. Indeed, using INMS results from atmospheric entry, Chadney et al. (2022) found that the addition of an influx of CH_4 into Saturn's thermosphere leads to photodissociated products in the region that could contribute to further chemistry and lead to the formation of higher mass molecules. Furthermore, Koskinen et al. (2016) previously highlighted the idea of CH_4 photochemistry in the lower region of Saturn's ionosphere to initiate the chemistry that produces benzene and ultimately polycyclic aromatic HC and stratospheric haze in Saturn. An in-depth analysis of the photochemical and compositional consequences of this exogenous material deeper in Saturn's atmosphere is beyond the scope of this paper.

5. Mixing Ratio and Density Determinations

After fitting the spectra using the mass spectral deconvolution described above, we use the results to determine the atmospheric mixing ratio and density of species included in the database. We follow the same method used in our previous work (Serigano et al., 2020). To determine these values one must take into account the electron impact ionization cross section, σ, which is unique to each species and quantifies the probability of a species to ionize within the instrument. Values for σ can be found in Table 1 and are calculated using the semiempirical formula defined in Fitch and Sauter (1983):

$$\sigma = 0.082 + \sum_{i=1}^{8} \alpha_i n_i \quad (7)$$

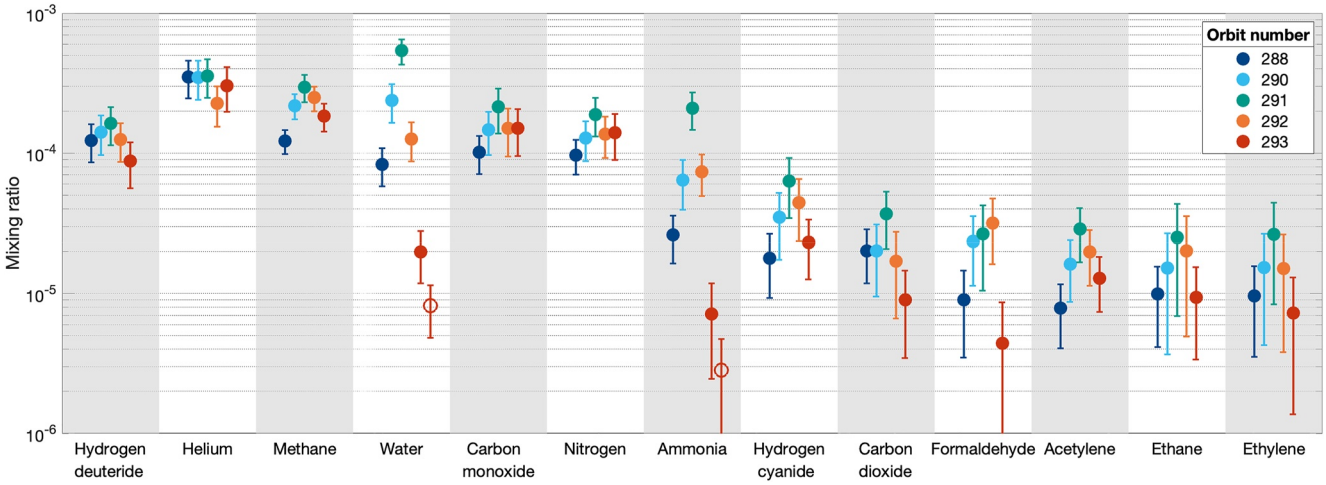

Figure 6. Mixing ratio results for the average mass spectrum for all orbits analyzed in this study. Average mass spectra include measurements taken between ϕ of 6.69 and 6.66×10^8 J kg^{-1} (~1,700–2,050 km). The species included here are all species aside from H_2 with a mixing ratio above 10^{-5} after averaging the results of all orbits. Results for H_2O and NH_3 for orbit 293 include both adsorption-corrected (filled data point) and uncorrected (unfilled data point) values. Error bars are a combination of 1σ uncertainties from counting statistics and 1σ uncertainties from the mass spectral deconvolution.

where α_i is a coefficient corresponding to each element and n_i is the number of atoms for that element. This equation is valid for small molecules composed of H, C, N, O, F, Cl, Br, or I atoms, which makes it suitable for our analysis. After taking the ionization cross sections into account, we can calculate atmospheric mixing ratios for each species based on the relative contribution of each species to the mass spectrum as determined by our modeling efforts. We calculate mixing ratios for the averaged mass spectra as well as the ϕ binned mass spectra. The averaged mass spectra, which utilize signal in the same region of Saturn from ϕ of 6.69 to 6.66×10^8 J kg^{-1}, allow us to directly compare measurements from each orbit. Results for the most abundant species in our analysis are shown in Figure 6. The species presented in this figure include all species with mixing ratios above 10^{-5} after averaging the results of all orbits. H_2, which is not included in this figure, always has a mixing ratio greater than 0.998. Mixing ratio results for all species and all orbits can be found in Table S2 in Supporting Information S1. Error bars are a combination of 1σ uncertainties from counting statistics from the data and 1σ uncertainties from the modeling results for each species.

H_2, HD, and He, which are native to Saturn, show less orbital variability when compared to the other most abundant species in the fit. The HD mixing ratio among orbits ranges from 8.9×10^{-5} to 1.6×10^{-4} with an orbital average of $1.3 \pm 0.4 \times 10^{-4}$, and the He mixing ratio ranges from 2.3×10^{-4} to 3.6×10^{-4} with an orbital average of $3.2 \pm 0.9 \times 10^{-4}$. The mixing ratios reported here are not representative of Saturn's bulk atmospheric mixing ratios since these measurements were taken in Saturn's upper thermosphere and well above the homopause. The majority of the remaining spectra are dominated by ices likely originating from the rings and falling into Saturn's atmosphere. CH_4 and H_2O are the next most abundant species, with average mixing ratios of $2.1 \pm 0.4 \times 10^{-4}$ and $2.0 \pm 0.5 \times 10^{-4}$, respectively, followed by CO, N_2, and NH_3. We include both corrected (filled data point) and uncorrected (unfilled data point) values for orbit 293 for H_2O and NH_3, which suffer from adsorption in the instrument as previously described. Even with corrections to orbit 293, H_2O and NH_3 are still severely depleted. Orbit 293 sampled a different latitudinal region of Saturn at the closest approach (9°N, compared to 5°S for other orbits) and did not cross the ring plane, which could explain the observed depletion in these measurements. The depletion and overall large variability with these species could also be due to other factors, which will be discussed in the following subsection.

Figure 7 shows the mixing ratio results after binning the data using ϕ bins of 0.01×10^8 J kg^{-1} and running each bin section as a separate mass spectrum. The corresponding pressure and altitude above the 1 bar pressure level are presented on the right y-axis. This provides a profile that allows for a better sense of any deviations among the species. Orbit 293 measurements extend down further than the other orbits since the spacecraft probed lower into Saturn's atmosphere before loss of signal. The extent of our ϕ binned analysis depends on the strength of the signal at higher altitudes (lower ϕ) and we utilize counts as long as the signal-to-noise ratio is sufficient for

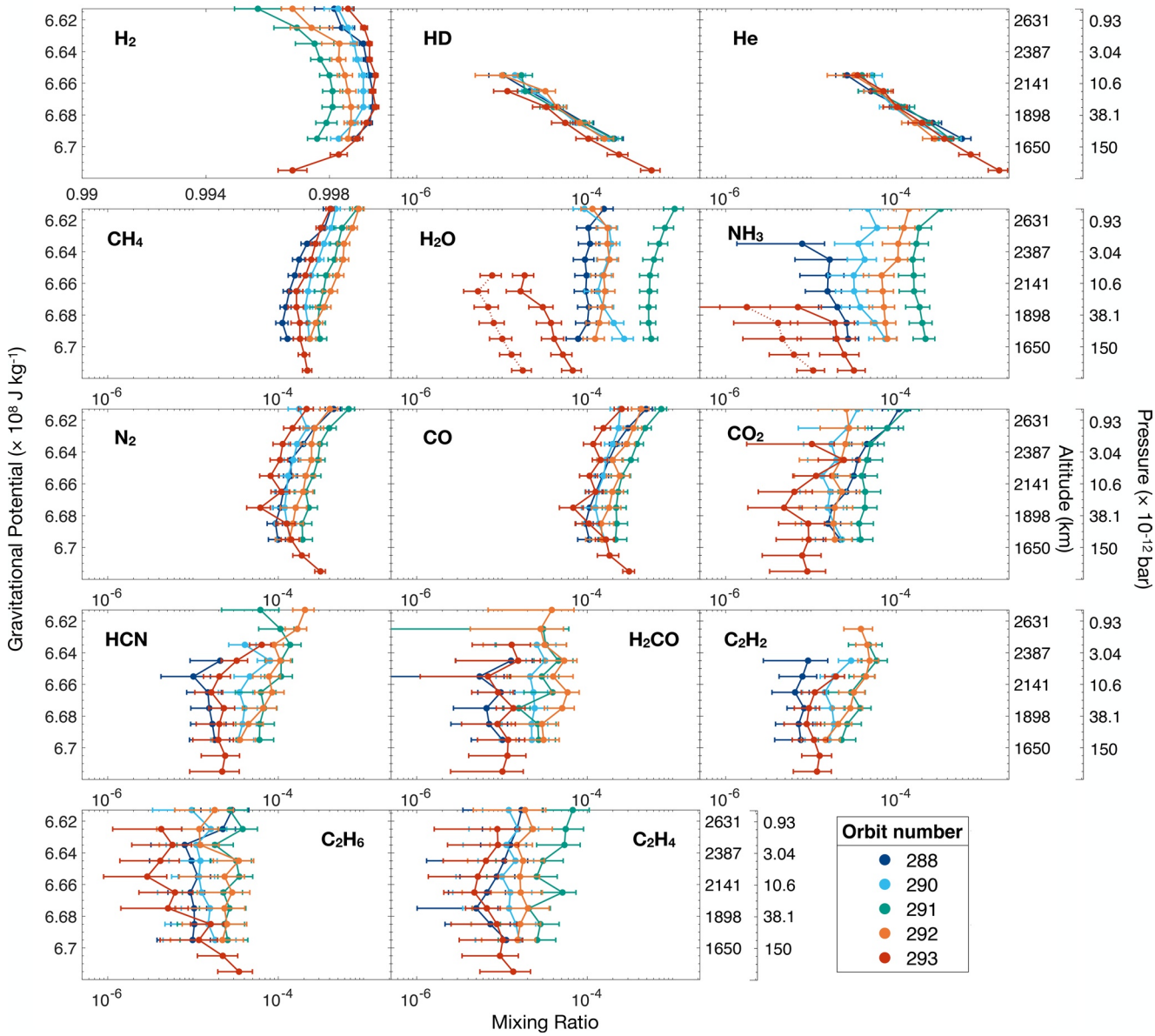

Figure 7. Inbound mixing ratio profiles of the most abundant species in our mass spectral fits. Profiles are constructed by averaging Ion and Neutral Mass Spectrometer measurements in gravitational potential bins of 0.01×10^8 J kg^{-1} and performing a mass spectral deconvolution for each individual bin. Results for H_2O and NH_3 for orbit 293 include both adsorption-corrected (solid line) and uncorrected (dotted line) values. Error bars are a combination of 1σ uncertainties from counting statistics and 1σ uncertainties from the mass spectral deconvolution.

analysis. The H_2 mixing ratio profile (upper left subfigure) decreases in the lower section due to the increasing abundances of other species, mainly HD and He, further into the planet. As the H_2 native to Saturn begins to decrease with height, the mixing ratio again decreases relative to the incoming material from the rings. Aside from HD and He, the mixing ratios of the other species are more or less constant, which is expected for species with a downward external flux into the atmosphere. However, the mixing ratios do slightly increase at the top and bottom of the profiles in response to the H_2 mixing ratio profile. HD and He decrease in abundance with increasing altitude, which is expected for native species following diffusive equilibrium above the homopause that are heavier in mass than an average atmospheric molecule. It should be noted that INMS cannot detect atomic H, which is expected to be an important constituent at these altitudes on Saturn. Due to the neglect of atomic H in this analysis, the mixing ratios discussed here are therefore mixing ratios of the measured constituents, rather

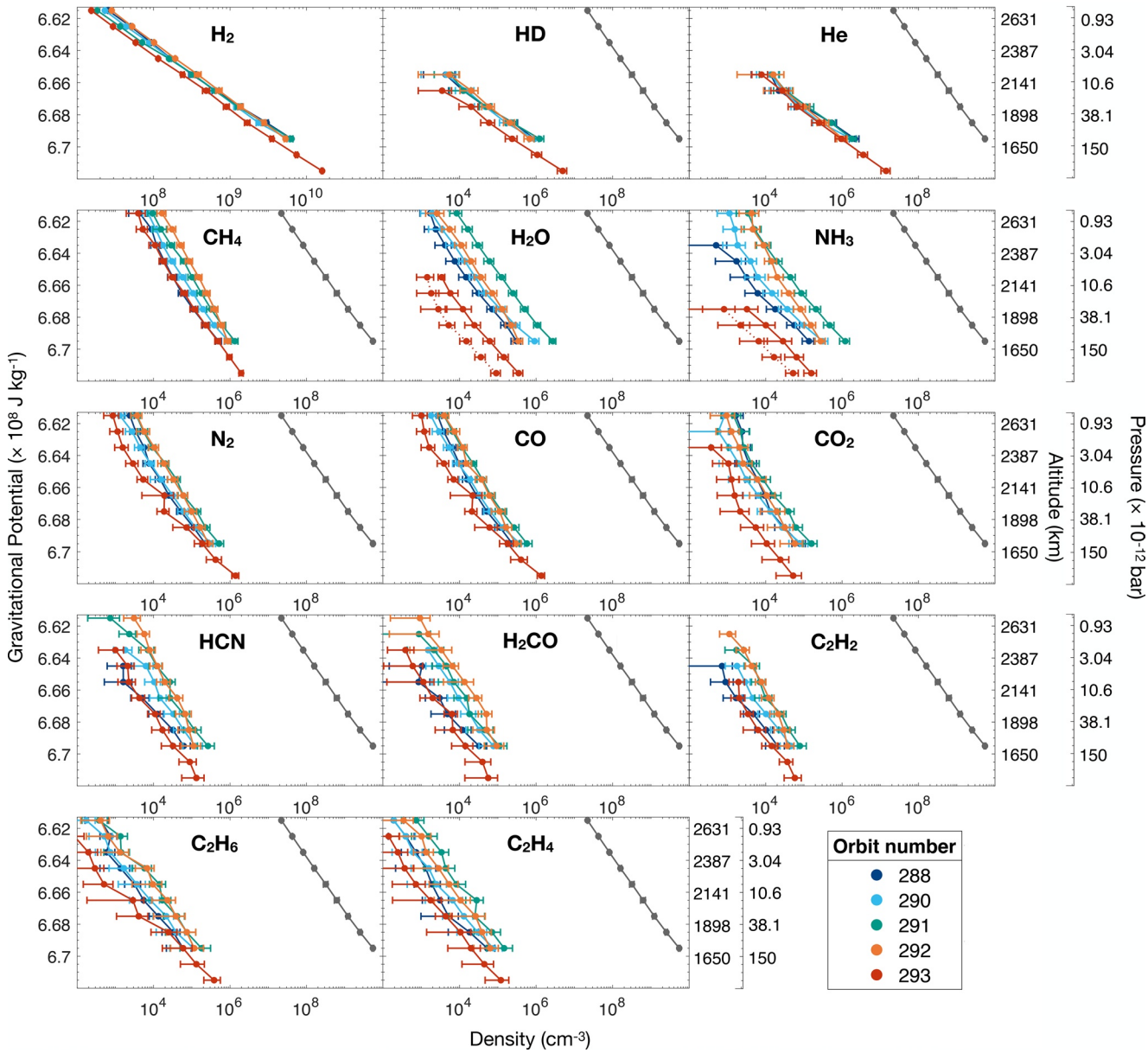

Figure 8. Inbound density profiles of the most abundant species in our mass spectral fits. The average H_2 density profile is plotted in gray on each subfigure to easily compare profiles. Profiles are constructed by averaging Ion and Neutral Mass Spectrometer measurements in gravitational potential bins of 0.01×10^8 J kg^{-1} and performing a mass spectral deconvolution for each individual bin. Results for H_2O and NH_3 for orbit 293 include both adsorption-corrected (solid line) and uncorrected (dotted line) values. Error bars are a combination of 1σ uncertainties from counting statistics and 1σ uncertainties from the mass spectral deconvolution.

than actual atmospheric mixing ratios, although the true atmospheric mixing ratios should be very similar to these values.

Similar to the mixing ratio profiles, we use our model results along with the corrections for sensitivity and ram enhancement discussed previously to determine density profiles for these species. We determine the density profiles for the most abundant species by weighting the count rate from the species' base peak with the relative contribution of that species returned by the model for each ϕ bin. Density results are shown in Figure 8. H_2 is plotted in the top left subfigure and the average H_2 density profile is plotted in all other subfigures to compare profiles. All species aside from HD and He follow a similar profile trend to H_2, again indicative of an external source for these species, while HD and He follow the trend of a species diffusively separating above the homopause.

Table 3
Comparison of Orbit 290–292 Average Mixing Ratios of Most Abundant Species From This Paper and Miller et al. (2020)

			Miller et al. (2020)			
Name	Formula	This paper	Auto fits[a]	Hydrocarbons[b]	ONS[c]	Average[d]
Hydrogen	H_2	0.99	0.999	0.998	0.998	0.998
Helium	He	3.1×10^{-4}	2.4×10^{-4}	2.4×10^{-4}	2.4×10^{-4}	2.4×10^{-4}
Methane	CH_4	2.6×10^{-4}	2.0×10^{-4}	2.3×10^{-4}	2.2×10^{-4}	2.3×10^{-4}
Water	H_2O	3.0×10^{-4}	3.6×10^{-4}	3.6×10^{-4}	3.6×10^{-4}	3.6×10^{-4}
Carbon monoxide	CO	1.7×10^{-4}	1.9×10^{-4}	–	–	2.5×10^{-5}
Nitrogen	N_2	1.5×10^{-4}	2.0×10^{-4}	–	1.2×10^{-4}	7.6×10^{-5}
Ammonia	NH_3	1.2×10^{-4}	2.1×10^{-4}	1.5×10^{-4}	1.5×10^{-4}	1.5×10^{-4}
Hydrogen cyanide	HCN	4.7×10^{-5}	6.9×10^{-5}	–	5.3×10^{-5}	5.3×10^{-5}
Carbon dioxide	CO_2	2.5×10^{-5}	–	–	–	3.4×10^{-6}
Formaldehyde	H_2CO	2.7×10^{-5}	2.0×10^{-5}	–	3.8×10^{-5}	3.8×10^{-5}
Acetylene	C_2H_2	2.2×10^{-5}	–	–	–	4.7×10^{-6}
Ethane	C_2H_6	2.0×10^{-5}	–	5.8×10^{-5}	–	4.5×10^{-5}
Ethylene	C_2H_4	1.9×10^{-5}	–	–	–	3.2×10^{-5}
Isobutane	C_4H_{10}	4.4×10^{-6}	–	6.1×10^{-4}	5.0×10^{-4}	6.7×10^{-4}
Propane	C_3H_8	7.9×10^{-6}	–	5.4×10^{-5}	–	4.3×10^{-5}
Propargyl alcohol	C_3H_4O	0.90×10^{-8}	–	–	1.5×10^{-4}	1.5×10^{-4}

[a]Most abundant species from auto-fit analysis of Miller et al. (2020), presented in their Table 2. [b]Most abundant species from hydrocarbon hand-fit analysis of Miller et al. (2020), presented in their Table 1. [c]Most abundant species from O-,N-,S-rich (ONS) hand-fit analysis of Miller et al. (2020), presented in their Table 1. [d]Most abundant species from averaged hand-fits (combined hydrocarbon and ONS, where applicable) of Miller et al. (2020), presented in their Table S4.

Despite separate data reduction and mass spectral deconvolution techniques, the results presented in this analysis arrive at similar conclusions to previous reports exploiting the same data set (Miller et al., 2020; Waite et al., 2018). All analyses conclude that the major components of the signal include the low mass native Saturn species (H_2, HD, and He) as well as notable volatile ices in the outer solar system: H_2O, NH_3, CH_4, CO, N_2, and CO_2. We compare results here only to Miller et al. (2020) (M20) since they report mixing ratio values and provide a full explanation of their fitting routine and results. Differences in compositional results arise mostly in lower signal regions that are attributed to more minor species in our database, which is unsurprising given the major differences in techniques involved with each analysis. While M20 provide a compositional auto-fit analysis comprising all species in the NIST mass spectral library with a mass under 100 amu (1,996 species in total), the database in this study includes only 80 species that we deem likely to be present in the spectrum based on our understanding of the sampled environment. M20 also include a "hand fit" analysis designed to produce endmember cases that include primarily HC or primarily O-,N-,S-rich (ONS) species in each fit and prioritize the attribution of signal based on knowledge of the environment. Instead of prioritizing certain species in our fit, which could influence the final result and increase the abundance of particular species, we fit all species in each region simultaneously. Importantly, since NIST calibration data is not a perfect substitute when INMS calibration data do not exist, we allow fragmentation peak intensities to vary throughout our deconvolution, as described above. We believe this new method of mass spectral deconvolution is a powerful new tool that can increase the scientific retrieval of planetary mass spectrometry data when calibration of the instrument is not sufficient.

A direct comparison of mixing ratio results for the most abundant species in this study and in M20 is found in Table 3. These values represent the averaged mixing ratio results for orbits 290–292. Missing values indicate species for which M20 did not report the mixing ratio value for that particular fitting scenario. The average column represents the most abundant species from averaging all hand-fit scenarios, including HC and ONS fits where applicable. Auto-fit results from M20 are the most directly comparable scenarios to our results since auto-fits incorporate all possible species into the fitting procedure and do not focus on endmember cases like the

HC and ONS fits, which omit certain species that could be present. Results from both studies are mostly similar, especially when comparing to the auto-fit values. Deviations among results do exist and occur mostly when comparing our results to the hand-fit endmember cases. One major discrepancy is isobutane (C_4H_{10}), which has a mixing ratio two orders of magnitude higher in M20 hand-fits but is not considerably abundant in their auto-fits or in our results. However, they report that the high mixing ratio of isobutane should be considered a tracer of an overall organic-rich composition and not specifically a high abundance of isobutane. Propane (C_3H_8) and propargyl alcohol (C_3H_4O) are two additional species with an important contribution to endmember cases in M20 that are notably much less abundant in our results and in their auto-fit results. The low abundance of propargyl alcohol in our results, for example, is due to the prominent contributions of higher mass species to the signal at *m/z* 55, the base peak of propargyl alcohol. The signal attributed to these high mass species at *m/z* 55 is slightly inflated in our results due to the lack of other high mass species in our database that would contribute to the same mass channels as these species. These high mass species include 1-hexene, 2-methyl-butane, and 3-methyl-1-butene, of which only 1-hexene is included in the M20 hand-fits.

CO and CO_2 are two important species in our results that should also be discussed in the context of results from M20. While CO adds a significant contribution to our best-fitting spectra and to their auto-fit results, results from their hand-fits are on average an order of magnitude lower and their CO results include a large range in potential mixing ratio values, $(0.002–2) \times 10^{-4}$. Nevertheless, our results are consistent and further emphasize the difficulty in breaking the degeneracies involved with analyzing unit resolution mass spectra. The highest CO_2 mixing ratio result from M20 is 6×10^{-6}, which is about a factor of four lower than our average CO_2 results listed in Table 3. M20 uses *m/z* 22 to constrain an upper limit for CO_2. Although we do not set any CO_2 constraints based on the *m/z* 22 signal, it should be noted that our model appropriately fits the *m/z* 22 signal in all instances.

5.1. Variability

Non-native species exhibit a greater overall variability from orbit to orbit, which is likely a consequence of the time variability in the ring source region or atmospheric dynamics associated with this very tenuous region. Measurements were taken at similar latitude and similar local solar time (aside from atmospheric entry) but did have a larger longitudinal range (see Table S1 in Supporting Information S1). Additionally, temporal variations could affect these results as these measurements were taken over the course of about a month from August to September of 2017. This region is exposed to the fluctuating solar wind, magnetospheric plasma, and other high energy phenomena, which could impart excess energy into the region and change the temperature, dynamics, and chemistry affecting the inner rings. Any fluctuations could lead to varying amounts of infalling ring material as observed using the instrument. Also, as first noted by Waite et al. (2018), dynamical disruptions in the area, such as the D68 ringlet disruption noted in Hedman et al. (2014), may cause local disturbances that influence the influx of material.

As discussed in Serigano et al. (2020), the volatility and proton affinity of these species could play a role in the observed variability and could also be responsible for the surprising prevalence of non-water ice and high mass organics in the spectra. Figure 9 shows the sublimation vapor pressure of the most abundant species at ring relevant temperatures of approximately 80–115 K (Filacchione et al., 2014; Tiscareno et al., 2019) taken from Fray and Schmitt (2009). Energetic events or disruptions in the area will lead to the liberation of molecules from larger ring particles, and a molecule's ability to recondense back onto a ring particle after liberation is highly dependent on the sublimation vapor pressure. At ring relevant temperatures, N_2, CO, and CH_4, the most abundant non-water ices in our fit, have the highest sublimation vapor pressures. It is possible that these species are being preferentially lost into Saturn from the rings since their high sublimation vapor pressures make it difficult to recondense back onto a ring particle. On the other hand, H_2O has the lowest sublimation vapor pressure and can more easily recondense back onto a ring particle and evade loss into Saturn's atmosphere, which could explain why the abundance of H_2O is relatively low when compared to other volatile species from the rings, given its dominance in the ring material. It is also possible that clathrate hydrate is present in the rings, with N_2, CO, CH_4, and other volatiles incorporated within the rings' dominant H_2O ice. This could explain the previous nondetection of significant amounts of non-water ice volatiles in the rings.

The proton affinity of a species could also affect the abundances observed by INMS. Proton affinities of the most abundant non-native species are taken from Hunter and Lias (1998) and can be found in Table 4. A species with a

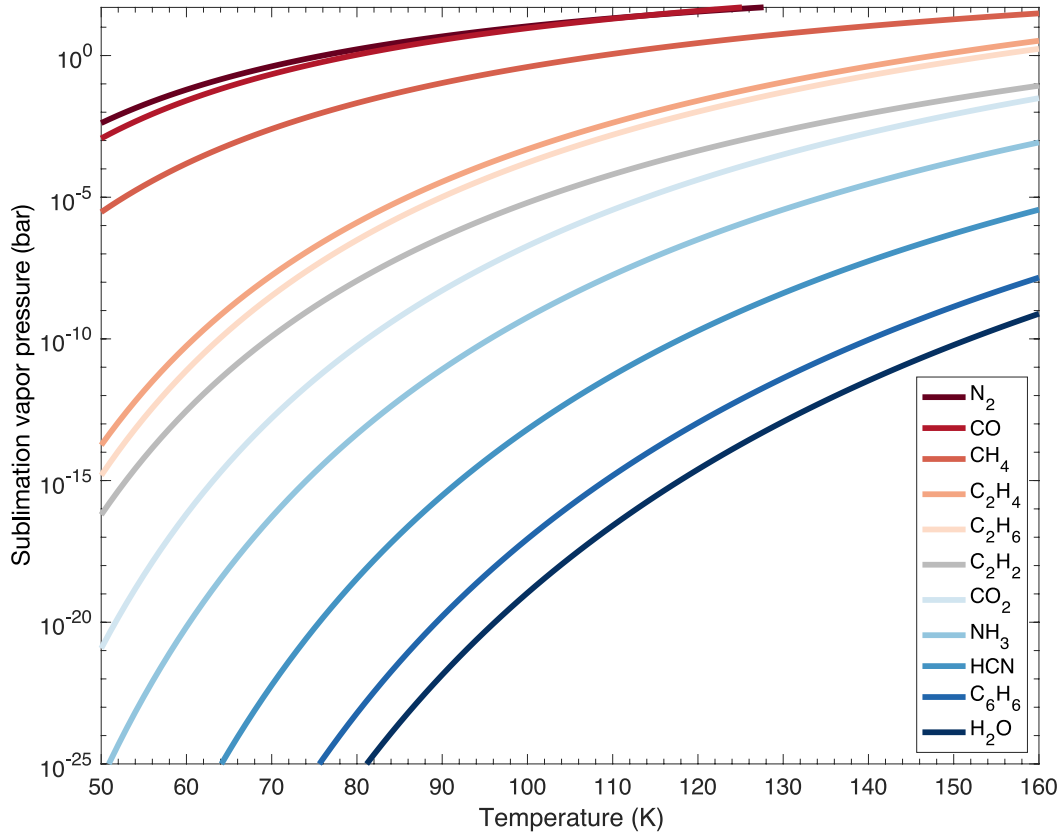

Figure 9. Sublimation vapor pressure curves for the most abundant non-native species in our mass spectral fits at temperatures relevant to Saturn's rings. Values in this figure are taken from Fray and Schmitt (2009). H_2CO is not included in this figure due to a lack of relevant data (see Fray & Schmitt, 2009).

higher proton affinity is more likely to be protonated after liberation from a ring particle. Most protonated molecules would evade detection by INMS in the CSN mode since the instrument is only sensitive to neutral molecules in this mode. (As CSN does not actively reject ions, we cannot rule out that a small portion of the signal is from ions that enter the instrument and are transformed in the antechamber and contribute to the neutral signal.) Thus, it is possible that species such as H_2O and NH_3, which have higher proton affinities, are entering Saturn's atmosphere in a charged form (e.g., H_3O^+ and NH_4^+) and not being detected by INMS. CH_4, CO, and N_2, on the other hand, are the most abundant non-water volatiles and have some of the lowest proton affinities compared to other abundant volatiles. Unfortunately, the INMS OSI mode was only able to measure up to *m/z* 8 due to the high speed of the spacecraft during the last orbits, so detection of larger ions from in situ measurements is not possible (Cravens et al., 2019). Remote observations do suggest that charged H_2O from the rings is entering Saturn's atmosphere. Ground-based observations from the Keck telescope discovered variations in Saturn's midlatitude H_3^+ intensity that they attribute to the presence of charged species derived from H_2O that were transported to Saturn's midlatitudes via regions of the rings that are magnetically linked to the atmosphere (O'Donoghue et al., 2013, 2017, 2019). Further ground- and space-based searches for definitive ion detections in this region would be very impactful. ALMA and JWST, with their unprecedented spectral and spatial resolutions, will certainly be able to improve our understanding of the relationship between Saturn's atmosphere and rings and the transport processes involved with this connection.

Table 4
Proton Affinities of the Most Abundant Non-Native Species, Taken From Hunter and Lias (1998)

Species	Proton affinity (kJ/mol)
NH_3	853.6
H_2CO	712.9
HCN	712.9
H_2O	691.0
C_2H_4	680.5
C_2H_2	641.4
C_2H_6	596.3
CO	594.0
CH_4	543.5
CO_2	540.5
N_2	493.8

Table 5
Temperature, Flux, and Mass Deposition Rate Results

Orbit number	Temperature (K)	Species	Flux ($\times 10^{12}$ m^{-2}s^{-1})	Mass deposition rate ($\times 10^{2}$ kg s^{-1})
288	368.8 ± 1.1	CO	15 ± 3.9	47 ± 12
		N_2	14 ± 3.1	44 ± 1.0
		H_2O	9.2 ± 2.6	18 ± 5.3
		CH_4	9.3 ± 1.7	16 ± 3.1
		CO_2	3.9 ± 1.6	19 ± 7.6
		HCN	2.7 ± 1.3	8.0 ± 3.8
		H_2CO	1.7 ± 1.0	5.8 ± 3.5
		NH_3	2.9 ± 1.0	5.4 ± 1.9
		C_2H_6	1.1 ± 0.6	3.8 ± 2.1
		C_2H_4	1.1 ± 0.7	3.4 ± 2.1
		C_2H_2	0.9 ± 0.4	2.5 ± 1.2
		Remaining	7.0 ± 1.2	44 ± 6.9
		Total	69 ± 6.5	218 ± 21
290	363.7 ± 1.0	CO	21 ± 7.1	67 ± 22
		N_2	18 ± 5.5	58 ± 17
		H_2O	26 ± 7.9	53 ± 16
		CH_4	17 ± 3.4	30 ± 6.1
		CO_2	3.8 ± 2.0	19 ± 9.7
		HCN	5.1 ± 2.6	16 ± 7.7
		H_2CO	4.4 ± 2.3	15 ± 7.6
		NH_3	7.1 ± 2.6	13 ± 5.0
		C_2H_6	1.7 ± 1.3	5.8 ± 4.4
		C_2H_4	1.7 ± 1.2	5.4 ± 3.9
		C_2H_2	1.8 ± 0.8	5.1 ± 2.4
		Remaining	18 ± 2.8	120 ± 19
		Total	126 ± 14	406 ± 41
291	339.6 ± 1.2	CO	32 ± 11	100 ± 35
		N_2	28 ± 8.5	88 ± 26
		H_2O	61 ± 12	120 ± 25
		CH_4	23 ± 5.0	41 ± 8.9
		CO_2	7.4 ± 3.2	36 ± 16
		HCN	9.7 ± 4.4	29 ± 13
		H_2CO	5.2 ± 3.1	17 ± 10
		NH_3	23 ± 6.9	45 ± 13
		C_2H_6	3.0 ± 2.1	10 ± 7.2
		C_2H_4	3.1 ± 2.1	9.6 ± 6.5
		C_2H_2	3.2 ± 1.3	9.3 ± 3.9
		Remaining	33 ± 4.1	231 ± 27
		Total	233 ± 22	741 ± 65
292	372.1 ± 1.0	CO	22 ± 8.0	68 ± 25
		N_2	20 ± 6.2	61 ± 19
		H_2O	14 ± 4.1	28 ± 8.2

6. Flux and Mass Deposition Rate of Ring Material Into Saturn

Similar to Serigano et al. (2020), we use the results from our mass spectral deconvolution to estimate the amount of material entering Saturn's atmosphere from the rings. We begin by determining the downward flux of the infalling species. The 1-D flux model used here is described in detail in Yelle et al. (2018) where it was used to determine the downward flux of CH_4 into Saturn's atmosphere. More recently, it was used in Serigano et al. (2020) to also determine the influx of H_2O and NH_3 into the atmosphere. We use the model here to determine the influx of all species originating from the rings using our analysis of the full mass range of the instrument. We assume hydrostatic equilibrium and solve the standard diffusion equation with ϕ as the vertical coordinate. The mixing ratio of a species is given by

$$X_i(\phi) = X_i(\phi_\circ)\exp\int_{\phi_\circ}^{\phi} d\phi' \frac{D_i}{D_i+K}\frac{m_i-m_a}{RT} - \int_{\phi_\circ}^{\phi} d\phi' \frac{F_i}{gN_a(D_i+K)}\exp\left(\int_{\phi_\circ}^{\phi} d\phi'' \frac{D_i}{D_i+K}\frac{m_i-m_a}{RT}\right) \quad (8)$$

where X_i is the mixing ratio of the minor constituent, D_i is the molecular diffusion coefficient, K is the eddy diffusion coefficient, m_i is the molecular mass of the minor constituent, m_a is the average molecular mass of the atmosphere, R is the gas constant for H_2, T is the temperature, g is the magnitude of the gravitational acceleration, N_a is the density of H_2, and F_i is the flux of the minor constituent. The first term of this equation represents molecular diffusion within the atmosphere and the second term describes the vertical distribution of a molecule with a nonzero external flux into the atmosphere.

The temperature profile for atmospheric entry that we use here can be found in Yelle et al. (2018). This was the only set of measurements that entered far enough into Saturn's atmosphere to detect a decrease in temperature at lower altitudes and was fit using a Bates' temperature profile for a thermosphere (Bates, 1951). All other orbits did not go deep enough to detect a temperature decrease and were fit using an isothermal model to the H_2 density. Additionally, we use the eddy diffusion coefficient from Yelle et al. (2018) of $K_\infty = 1.4 \times 10^4$ m^{2}s^{-1}. The molecular diffusion coefficient, D_i, is species specific and is taken from Mason and Marrero (1970) for He and CH_4 in H_2. For all other species it is calculated using the theoretical approach based on the Lennard-Jones potential found in Hirschfelder et al. (1954). More detail on the molecular diffusion coefficients can be found in Supporting Information S1.

We determine the downward flux for all of the major species discussed above. We again use the region of Saturn where all orbits have data, from ϕ of 6.69 to 6.66 $\times 10^8$ J kg^{-1}. In this region mixing ratios of external species are roughly constant, leading to a constant downward flux. HD and He, which are native to Saturn and should have no external flux, are able to be fit with a downward flux of 0 m^{-2}s^{-1}, as expected. All other major species are fit with a downward flux on the order of 10^{12}–10^{13} m^{-2}s^{-1}. These results can be found in Table 5. The remaining minor species in the database constitute a much lower signal than the previously discussed species, representing an average combined mixing ratio of only 6.3 $\times 10^{-5}$. The flux of these species, along with the MDRs discussed below, are calculated for each species separately and are reported here as combined values. Since the parameters needed to

Table 5
Continued

Orbit number	Temperature (K)	Species	Flux ($\times 10^{12}$ m^{-2}s^{-1})	Mass deposition rate ($\times 10^{2}$ kg s^{-1})
		CH_4	19 ± 3.7	34 ± 6.6
		CO_2	3.2 ± 1.9	16 ± 9.4
		HCN	6.5 ± 3.0	20 ± 9.1
		H_2CO	5.9 ± 2.9	20 ± 9.6
		NH_3	8.0 ± 2.5	15 ± 4.8
		C_2H_6	2.3 ± 1.7	7.7 ± 5.8
		C_2H_4	1.7 ± 1.3	5.3 ± 3.9
		C_2H_2	2.1 ± 0.9	6.2 ± 2.6
		Remaining	21 ± 3.3	142 ± 22
		Total	125 ± 13	423 ± 44
293	351.1 ± 1.2	CO	23 ± 6.2	72 ± 19
		N_2	21 ± 5.5	66 ± 17
		H_2O	2.3 ± 0.7	4.6 ± 1.5
		CH_4	15 ± 3.2	26 ± 5.6
		CO_2	1.8 ± 1.1	9.0 ± 5.2
		HCN	3.6 ± 1.5	11 ± 4.5
		H_2CO	0.9 ± 1.0	2.9 ± 3.3
		NH_3	0.8 ± 0.5	1.5 ± 0.9
		C_2H_6	1.1 ± 0.7	3.8 ± 2.2
		C_2H_4	0.9 ± 0.7	2.7 ± 2.1
		C_2H_2	1.5 ± 0.5	4.2 ± 1.5
		Remaining	9.0 ± 3.1	50 ± 16
		Total	81 ± 9.7	254 ± 32

Note. The "Remaining" value represents the results of the remaining minor species in the database, which constitute a much lower signal than the previously reported species and are reported here as combined flux and mass deposition rate values.

determine the theoretical molecular diffusion coefficient are not always available in the literature, the molecular diffusion coefficient we use for the combined influx calculation of minor species is the average diffusion coefficient used for the major species. Since the molecular diffusion coefficient does not vary widely among the major species, this is an appropriate approximation when the needed parameters are not available.

Our total influx results range from 6.9×10^{13} to 2.3×10^{14} m^{-2}s^{-1}, which is a considerable and unsustainable amount of material from the rings. We quantify the amount of material being deposited into the atmosphere from the rings by converting these flux values into MDRs, following the same method as Serigano et al. (2020). We approximate the MDRs using the equation:

$$MDR = F_i m_i \times 2\pi r_{Saturn}^2 \theta, \quad (9)$$

where F_i is the flux of molecule i, m_i is the molecular mass of molecule i, and θ represents the latitudinal width for the influx region. We choose a latitudinal width of ±8° from the ring plane, which corresponds to the region where most of the major constituents are above the noise level. It is possible that the latitudinal extent is broader than this; however, we do not have sufficient signal further from the ring plane to determine this. Results from this calculation are also found in Table 5.

We calculate a total MDR on the order of 10^4 kg/s, with results ranging from 2.2 to 7.4×10^4 kg/s. Since this calculation depends on the mass of individual molecules entering the atmosphere, it is worth noting that species with the highest mixing ratios are not necessarily the species that contribute the most to this mass calculation. On average, CO and N_2 provide the largest contribution by mass to these results, followed by H_2O, CH_4, and CO_2. Results of the total mass contribution are similar to previous estimates from Waite et al. (2018) (0.5–4.5×10^4 kg/s) and Perry et al. (2018) (1–20×10^4 kg/s). Slight differences in these results are not surprising, given that this is a completely independent analysis using different methods. Waite et al. (2018) determine a downward diffusion velocity based on a limiting flux equation (and alternatively by using a hydrostatic model to determine diffusion coefficients) and calculate a mass influx based on an 8° latitudinal width for the influxing region. Perry et al. (2018) use a latitudinal width of 20° and determine the diffusion velocity of an infalling molecule by assuming that the material entering Saturn's atmosphere is settling in the Epstein regime by viscous drag, which allows them to calculate the diffusion velocity as the terminal velocity. Regardless of differences in calculating these values, all independent analyses of this data set have arrived at the conclusion that the amount of influx from the rings is surprisingly large and unsustainable over a long period of time.

Recent gravity measurements from the Grand Finale orbits estimate the total mass of the rings to be $1.54 \pm 0.49 \times 10^{19}$ kg (Iess et al., 2019). Although the total mass of the rings is well constrained, individual ring masses are not as well determined due to the correlations among the rings. Iess et al. (2019) estimate the C ring to be approximately 0.024 Mimas masses, which agrees with previous estimates from UVIS stellar occultations (Baillié et al., 2011). The D ring is assumed to be no more than 1% of the total mass of the C ring (Waite et al., 2018), bringing the estimated mass of the D ring to 9×10^{15} kg and the combined mass of the C and D rings to 9.09×10^{17} kg. If the MDR determined by INMS measurements is a constant source of influx into Saturn's atmosphere, the entire D ring would be depleted in a matter of thousands of years. It is likely that the C ring supplies material to the D ring over time via viscous spreading or other energetic events that perturb the rings. Assuming this is an efficient process, the combined C and D rings would only last on the order of 10^5–10^6 years. Our assumptions here are straightforward and assume that all material in these rings would act in a similar manner to the material detected by INMS, which we know is not the case. It is likely that our simplified timescale calculations are more of a lower limit; however, a more elaborate analysis of ring dynamics as related to mass

loss into Saturn is beyond the scope of this paper. The lifetimes we report here are extremely small on planetary timescales and combined with recent estimates of the age of the rings (≤150 Myr). Zhang et al. (2017b) suggest that deposition of large amounts of ring material reported here is likely not representative of the typical influx over the lifetime of the ring system. This further suggests that the massive influx is likely a transient phenomenon that could be a consequence of recent perturbations in this region, such as the D68 disturbance noted in Hedman et al. (2014).

7. Conclusions

Cassini's Grand Finale orbits provided a unique opportunity to probe the region between Saturn and the D ring and the unexpected complexity of the mass spectra returned by INMS sheds light on the intricate coupling between Saturn's atmosphere and rings. Five orbits that sampled Saturn's thermosphere directly allowed for an in-depth in situ analysis of the composition of this region, with INMS returning rich spectra full of components native to Saturn (H_2, HD, and He) as well as ices and higher mass organics likely originating from the rings and falling into the atmosphere. In this paper, we expanded on our previous work (Serigano et al., 2020; Yelle et al., 2018) to provide an in-depth analysis of the signal from the entire mass range returned by INMS for Cassini orbits 288, 290, 291, 292, and 293. While most orbits returned similar mass spectra, orbit 291 included more exogenous material than others while orbit 293 was depleted in many exogenous species, namely H_2O and NH_3. Orbit 293 included the only set of measurements that probed a different latitudinal region of Saturn, which could be responsible for the differences between this orbit and the rest.

Deconvolving a unit resolution mass spectrum to determine the constituents present in the signal is a degenerate process since fragments from different species overlap and contribute to the same mass channels. The lack of INMS calibration data for many species of interest further complicates the process. After creating a database of 80 species to fit the mass spectra, we adopt a mass spectral deconvolution tool that uses Monte Carlo randomization to vary the peak intensities of each fragment to fit the measurements (Gautier et al., 2020). We perform this deconvolution for an averaged mass spectrum of each orbit between ϕ of 6.69 and 6.66×10^8 J kg^{-1} to directly compare results as well as vertically resolved mass spectra determined over a ϕ bin resolution of 0.01×10^8 J kg^{-1} to retrieve the mixing ratio and density profiles of all major species.

Native Saturn species, H_2, HD, and He, behave as expected for atmospheric constituents in diffusive separation above an atmosphere's homopause. Our best-fitting measurements attribute much of the signal at lower masses to ices, namely CH_4, NH_3, H_2O, CO, N_2, and CO_2, and the bulk of the higher mass signal to organics. These species likely originate in the rings, but the possibility of some constituents being products of photochemistry in the upper thermosphere is not excluded, although the constant mixing ratios with respect to H_2 as a function of altitude suggest that diffusion dominates over any photochemical production. We rule out contamination from previous INMS targets as the source of this material since the spectra returned from all targets differ significantly in certain regions. The total influx of material from the rings amounts from 6.9×10^{13} to 2.3×10^{14} m^{-2}s^{-1}, which translates to a MDR of 2.2–7.4 $\times 10^4$ kg/s of material entering Saturn's atmosphere from the rings. This is a significant amount of material and is an unsustainable loss from the rings over long timescales, suggesting that the influx measured here could be a transient phenomenon due to recent perturbations in the region such as the D68 disruption noted by Hedman et al. (2014).

Future photochemical modeling of this region utilizing the results presented in this analysis is crucial in understanding the processes at play in this unique, interconnected region of our solar system. The unexpectedly complex composition found in Saturn's upper thermosphere could have implications for the radiative balance and dynamics of the region, and even haze production at deeper levels in the stratosphere, given that several of these molecules would be expected to condense in Saturn's colder lower stratosphere. Without Cassini's presence in the Saturn system, future in situ measurements of this region may be decades away. We must rely on ground- and space-based observatories such as ALMA and JWST to help illuminate the many outstanding questions pertaining to Saturn's ring-atmosphere coupling.

Data Availability Statement

The original INMS data analyzed here are archived in the Planetary Data System and can be accessed directly at https://pds-ppi.igpp.ucla.edu/search/view/?f=yes&id=pds://PPI/CO-S-INMS-3-L1A-U-V1.0/DATA/SATURN/2017 (Waite et al., 2005). Data generated as a result of this analysis are available in the Johns Hopkins University Data Archive with the following https://doi.org/10.7281/T1/LJ9FLW (Serigano et al., 2022).

Acknowledgments
This research was supported by Grant Number 80NSSC19K0903 and 80NSSC17M0008 originally selected as part of the Cassini Data Analysis Program, and now supported by NASA's Planetary Science Division Internal Scientist Funding Program through the Fundamental Laboratory Research (FLaRe) work package.

References

Baillié, K., Colwell, J. E., Lissauer, J. J., Esposito, L. W., & Sremčević, M. (2011). Waves in Cassini UVIS stellar occultations: 2. The C ring. *Icarus*, *216*(1), 292–308. https://doi.org/10.1016/j.icarus.2011.05.019

Bates, D. R. (1951). The temperature of the upper atmosphere. *Proceedings of the Physical Society Section B*, *64*(9), 805–821. https://doi.org/10.1088/0370-1301/64/9/312

Chadney, J., Koskinen, T. T., Hu, X., Galand, M., Lavvas, P., Unruh, Y., et al. (2022). Energy deposition in Saturn's equatorial upper atmosphere. *Icarus*, *372*, 114724. https://doi.org/10.1016/j.icarus.2021.114724

Ciarniello, M., Filacchione, G., D'Aversa, E., Capaccioni, F., Nicholson, P., Cuzzi, J., et al. (2019). Cassini-VIMS observations of Saturn's main rings: II. A spectrophotometric study by means of Monte Carlo ray-tracing and Hapke's theory. *Icarus*, *317*, 242–265. https://doi.org/10.1016/j.icarus.2018.07.010

Connerney, J. E. P., & Waite, J. H. (1984). New model of Saturn's ionosphere with an influx of water from the rings. *Nature*, *312*(5990), 136–138. https://doi.org/10.1038/312136a0

Cravens, T. E., Moore, L., Waite, J. H., Perryman, R., Perry, M., Wahlund, J. E., et al. (2019). The ion composition of Saturn's equatorial ionosphere as observed by Cassini. *Geophysical Research Letters*, *46*(12), 6315–6321. https://doi.org/10.1029/2018gl077868

Cruikshank, D. P., Roush, T. L., Owen, T. C., Geballe, T. R., De Bergh, C., Schmitt, B., et al. (1993). Ices on the surface of Triton. *Science*, *261*(5122), 742–745. https://doi.org/10.1126/science.261.5122.742

Cui, J., Yelle, R. V., Vuitton, V., Waite, J. H., Kasprzak, W. T., Gell, D. A., et al. (2009a). Analysis of Titan's neutral upper atmosphere from Cassini Ion Neutral Mass Spectrometer measurements. *Icarus*, *200*(2), 581–615. https://doi.org/10.1016/j.icarus.2008.12.005

Cuzzi, J. N., Filacchione, G., & Marouf, E. A. (2018). The rings of Saturn. In M. S. Tiscareno & C. D. Murray (Eds.), *Planetary ring systems: Properties, structure, and evolution* (pp. 51–92). Cambridge University Press. https://doi.org/10.1017/9781316286791.003

Cuzzi, J. N., French, R. G., Hendrix, A. R., Olson, D. M., Roush, T., & Vahidinia, S. (2018). HST-STIS spectra and the redness of Saturn's rings. *Icarus*, *309*, 363–388. https://doi.org/10.1016/j.icarus.2018.02.025

Diebold, U., & Madey, T. (1992). Adsorption and electron stimulated desorption of NH_3/TiO_2 (110). *Journal of Vacuum Science and Technology A: Vacuum, Surfaces, and Films*, *10*(4), 2327–2335. https://doi.org/10.1116/1.577939

Filacchione, G., Ciarniello, M., Capaccioni, F., Clark, R. N., Nicholson, P. D., Hedman, M. M., et al. (2014). Cassini–VIMS observations of Saturn's main rings: I. Spectral properties and temperature radial profiles variability with phase angle and elevation. *Icarus*, *241*, 45–65. https://doi.org/10.1016/j.icarus.2014.06.001

Fitch, W. L., & Sauter, A. D. (1983). Calculation of relative electron impact total ionization cross sections for organic molecules. *Analytical Chemistry*, *55*(6), 832–835. https://doi.org/10.1021/ac00257a006

Fray, N., & Schmitt, B. (2009). Sublimation of ices of astrophysical interest: A bibliographic review. *Planetary and Space Science*, *57*(14–15), 2053–2080. https://doi.org/10.1016/j.pss.2009.09.011

Gautier, T., Serigano, J., Bourgalais, J., Hörst, S. M., & Trainer, M. G. (2020). Decomposition of electron ionization mass spectra for space application using a Monte-Carlo approach. *Rapid Communications in Mass Spectrometry*, *34*(8), e8684. https://doi.org/10.1002/rcm.8684

Goesmann, F., Rosenbauer, H., Bredehöft, J. H., Cabane, M., Ehrenfreund, P., Gautier, T., et al. (2015). Organic compounds on comet 67P/Churyumov-Gerasimenko revealed by COSAC mass spectrometry. *Science*, *349*(6247), aab0689. https://doi.org/10.1126/science.aab0689

Grundy, W., Binzel, R., Buratti, B., Cook, J., Cruikshank, D., Dalle Ore, C., et al. (2016). Surface compositions across Pluto and Charon. *Science*, *351*(6279). https://doi.org/10.1126/science.aad9189

Hamil, O., Cravens, T., Reedy, N. L., & Sakai, S. (2018). Fate of ice grains in Saturn's ionosphere. *Journal of Geophysical Research: Space Physics*, *123*(2), 1429–1440. https://doi.org/10.1002/2017ja024616

Hedman, M. M., Burt, J. A., Burns, J. A., & Showalter, M. R. (2014). Non-circular features in Saturn's D ring: D68. *Icarus*, *233*, 147–162. https://doi.org/10.1016/j.icarus.2014.01.022

Hirschfelder, J. O., Curtiss, C. F., Bird, R. B., & Mayer, M. G. (1954). *Molecular Theory of Gases and Liquids* (Vol. 26). Wiley.

Hörst, S. M. (2017). Titan's atmosphere and climate. *Journal of Geophysical Research: Planets*, *122*(3), 432–482. https://doi.org/10.1002/2016je005240

Hsu, H.-W., Schmidt, J., Kempf, S., Postberg, F., Moragas-Klostermeyer, G., Seiß, M., et al. (2018). In situ collection of dust grains falling from Saturn's rings into its atmosphere. *Science*, *362*(6410), eaat3185. https://doi.org/10.1126/science.aat3185

Hunter, E. P. L., & Lias, S. G. (1998). Evaluated gas phase basicities and proton affinities of molecules: An update. *Journal of Physical and Chemical Reference Data*, *27*(3), 413–656. https://doi.org/10.1063/1.556018

Iess, L., Militzer, B., Kaspi, Y., Nicholson, P., Durante, D., Racioppa, P., et al. (2019). Measurement and implications of Saturn's gravity field and ring mass. *Science*, *364*(6445), eaat2965. https://doi.org/10.1126/science.aat2965

Koskinen, T., Moses, J., West, R., Guerlet, S., & Jouchoux, A. (2016). The detection of benzene in Saturn's upper atmosphere. *Geophysical Research Letters*, *43*(15), 7895–7901. https://doi.org/10.1002/2016gl070000

Magee, B. A., Waite, J. H., Mandt, K. E., Westlake, J., Bell, J., & Gell, D. A. (2009). INMS-derived composition of Titan's upper atmosphere: Analysis methods and model comparison. *Planetary and Space Science*, *57*(14–15), 1895–1916. https://doi.org/10.1016/j.pss.2009.06.016

Mason, E. A., & Marrero, T. R. (1970). The diffusion of atoms and molecules. In *Advances in atomic and molecular physics* (Vol. 6, pp. 155–232). Elsevier.

Miller, K. E., Waite, J. H., Perryman, R. S., Perry, M. E., Bouquet, A., Magee, B. A., et al. (2020). Cassini INMS constraints on the composition and latitudinal fractionation of Saturn ring rain material. *Icarus*, *339*, 113595. https://doi.org/10.1016/j.icarus.2019.113595

Mitchell, D. G., Perry, M. E., Hamilton, D. C., Westlake, J. H., Kollmann, P., Smith, H. T., et al. (2018). Dust grains fall from Saturn's D-ring into its equatorial upper atmosphere. *Science*, *362*(6410), eaat2236. https://doi.org/10.1126/science.aat2236

Moore, L., Cravens, T. E., Müller-Wodarg, I. C. F., Perry, M. E., Waite, J. H., Perryman, R. S., et al. (2018). Models of Saturn's equatorial ionosphere based on in situ data from Cassini's Grand Finale. *Geophysical Research Letters*, *45*(18), 9398–9407. https://doi.org/10.1029/2018gl078162

O'Donoghue, J., Moore, L., Connerney, J., Melin, H., Stallard, T. S., Miller, S., & Baines, K. H. (2019). Observations of the chemical and thermal response of 'ring rain' on Saturn's ionosphere. *Icarus*, *322*, 251–260. https://doi.org/10.1016/j.icarus.2018.10.027

O'Donoghue, J., Moore, L., Connerney, J. E. P., Melin, H., Stallard, T. S., Miller, S., & Baines, K. H. (2017). Redetection of the Ionospheric signature of Saturn's 'ring rain'. *Geophysical Research Letters*, *44*(23), 11–762. https://doi.org/10.1002/2017gl075932

O'Donoghue, J., Stallard, T. S., Melin, H., Jones, G. H., Cowley, S. W. H., Miller, S., et al. (2013). The domination of Saturn's low-latitude ionosphere by ring 'rain'. *Nature*, *496*(7444), 193–195. https://doi.org/10.1038/nature12049

Perry, M. E., Teolis, B., Smith, H. T., McNutt, R. L., Fletcher, G. G., Kasprzak, W., et al. (2010). Cassini INMS observations of neutral molecules in Saturn's E-ring. *Journal of Geophysical Research*, *115*(A10). https://doi.org/10.1029/2010ja015248

Perry, M. E., Teolis, B. D., Hurley, D. M., Magee, B. A., Waite, J. H., Brockwell, T. G., et al. (2015). Cassini INMS measurements of Enceladus plume density. *Icarus*, *257*, 139–162. https://doi.org/10.1016/j.icarus.2015.04.037

Perry, M. E., Waite, J. H., Mitchell, D. G., Miller, K. E., Cravens, T. E., Perryman, R. S., et al. (2018). Material flux from the rings of Saturn into its atmosphere. *Geophysical Research Letters*, *45*(19), 10–93. https://doi.org/10.1029/2018gl078575

Serigano, J., Hörst, S., He, C., Gautier, T., Yelle, R., Koskinen, T., et al. (2022). Data associated with the publication: Compositional measurements of Saturn's upper atmosphere and rings from Cassini INMS: An extended analysis of measurements from Cassini's Grand Finale orbits. Johns Hopkins University Data Archive, V1.

Serigano, J., Hörst, S., He, C., Gautier, T., Yelle, R., Koskinen, T., & Trainer, M. (2020). Compositional measurements of Saturn's upper atmosphere and rings from Cassini INMS. *Journal of Geophysical Research: Planets*, *125*(8), e2020JE006427. https://doi.org/10.1029/2020je006427

Teolis, B. D., Perry, M. E., Magee, B. A., Westlake, J., & Waite, J. H. (2010). Detection and measurement of ice grains and gas distribution in the Enceladus plume by Cassini's Ion Neutral Mass Spectrometer. *Journal of Geophysical Research*, *115*(A9). https://doi.org/10.1029/2009ja015192

Tiscareno, M. S., Nicholson, P. D., Cuzzi, J. N., Spilker, L. J., Murray, C. D., Hedman, M. M., et al. (2019). Close-range remote sensing of Saturn's rings during Cassini's ring-grazing orbits and Grand Finale. *Science*, *364*(6445), eaau1017. https://doi.org/10.1126/science.aau1017

Wahlund, J. E., Morooka, M. W., Hadid, L. Z., Persoon, A. M., Farrell, W. M., Gurnett, D. A., et al. (2018). In situ measurements of Saturn's ionosphere show that it is dynamic and interacts with the rings. *Science*, *359*(6371), 66–68. https://doi.org/10.1126/science.aao4134

Waite, J. H., Kasprzak, W. T., Luhman, J. G., Cravens, T. E., Yelle, R. V., McNutt, R. L., et al. (2005). *CASSINI INMS level 1A extracted data V1.0*. NASA Planetary Data System. CO-S-INMS-3-L1A-U-V1.0.

Waite, J. H., Lewis, W. S., Kasprzak, W. T., Anicich, V. G., Block, B. P., Cravens, T. E., et al. (2004). The Cassini ion and neutral mass spectrometer (INMS) investigation. In *The Cassini-Huygens Mission* (pp. 113–231). Springer.

Waite, J. H., Lewis, W. S., Magee, B. A., Lunine, J. I., McKinnon, W. B., Glein, C. R., et al. (2009). Liquid water on Enceladus from observations of ammonia and ^{40}Ar in the plume. *Nature*, *460*(7254), 487–490. https://doi.org/10.1038/nature08153

Waite, J. H., Perryman, R. S., Perry, M. E., Miller, K. E., Bell, J., Cravens, T. E., et al. (2018). Chemical interactions between Saturn's atmosphere and its rings. *Science*, *362*(6410), eaat2382. https://doi.org/10.1126/science.aat2382

Wallace, W. (2022). Mass spectra. In P. Linstrom & W. Mallard (Eds.), *NIST Chemistry WebBook*. NIST Standard Reference Database Number 69. https://doi.org/10.18434/T4D303

Yelle, R. V., Serigano, J., Koskinen, T. T., Hörst, S. M., Perry, M. E., Perryman, R. S., & Waite, J. H. (2018). Thermal structure and composition of Saturn's upper atmosphere from Cassini/Ion Neutral Mass Spectrometer measurements. *Geophysical Research Letters*, *45*(20), 10–951. https://doi.org/10.1029/2018gl078454

Zhang, Z., Hayes, A., de Pater, I., Dunn, D., Janssen, M., Nicholson, P., et al. (2019). VLA multi-wavelength microwave observations of Saturn's C and B rings. *Icarus*, *317*, 518–548. https://doi.org/10.1016/j.icarus.2018.08.014

Zhang, Z., Hayes, A., Janssen, M., Nicholson, P., Cuzzi, J., de Pater, I., et al. (2017a). Cassini microwave observations provide clues to the origin of Saturn's C ring. *Icarus*, *281*, 297–321. https://doi.org/10.1016/j.icarus.2016.07.020

Zhang, Z., Hayes, A., Janssen, M., Nicholson, P., Cuzzi, J., de Pater, I., & Dunn, D. (2017b). Exposure age of Saturn's A and B rings, and the Cassini Division as suggested by their non-icy material content. *Icarus*, *294*, 14–42. https://doi.org/10.1016/j.icarus.2017.04.008